

C 1 Reduced Dimensions I: Magnetic Moment and Magnetic Structure

Stefan Blügel

Institut für Festkörperforschung

Forschungszentrum Jülich GmbH, D-52425 Jülich

Contents

1	Introduction	3
2	Theory and Models	4
2.1	Density Functional Theory: Non-collinear Magnetism	5
2.2	Heisenberg Model and Beyond	6
2.3	Stoner Model	8
2.4	Role of Coordination Number	10
3	Surfaces	14
3.1	General Overview	14
3.2	Example: Cr(100)	15
3.3	Example: V(100)	18
3.4	The (100)-Surfaces of VRu, VRh and VPd Alloys	18
4	Ultrathin Films	19
4.1	(100) Oriented Monolayers on Nonmagnetic Substrates	20
4.2	(111) Oriented Monolayers on Nonmagnetic Substrates	25
4.3	Magnetic Substrate: Magnetic Exchange Coupling of 3d Metals on Fe(001)	29
5	Atomic-Scale Structures	33
5.1	Adatoms	33
5.2	Clusters	34

1 Introduction

We explore the ground state magnetic properties of surfaces, ultrathin films and some atomic-scale structures with the attention to question which systems are magnetic and what is the magnetic ground-state structure.

In this article we focus on the dimensional aspect of itinerant magnetism, in particular of those systems including d electrons, as relevant for the magnetic ground-state properties of metallic surfaces, interfaces, multilayers, ultrathin films, step edges, or magnetic clusters deposited on surfaces. Considering the vast number of possible systems, a number growing fast with the number of constituent atoms, the surface and interface orientation, the chemical and structural roughness at interfaces, the electronic nature of the substrate (metal, semiconductor, insulator), an exhaustive review is unattainable. Instead we discuss chemical trends in order to develop an intuition helpful to understand also new systems or envisage new effects not investigated yet.

The simplest low-dimensional systems are isolated atoms, whose spin moments as function of the the number of d electrons are well described by Hund's first rule: the spins of all electrons are aligned in parallel as long as no quantum number is occupied more than once. Thus, nearly all of the 30 transition-metal atoms have magnetic spin moments. The largest possible d moments occur at the center of each series, i.e. $5 \mu_B$ for Cr and Mn in the $3d$ series. On the other hand, it is well-known that only 5 of 30 transition metals remain magnetic in their bulk crystalline phase: Co and Ni are ferromagnetic, Cr is antiferromagnetic, and Mn and Fe are ferromagnetic or antiferromagnetic depending on their crystal structure (cf. Fig. 1). Low-dimensional transition-metals should fall in between these two extremes. Magnetic material may be envisaged, which is nonmagnetic as bulk metal but magnetic as nano-structure. Although these arguments do apply, band narrowing, charge transfer, lift of degeneracies, structural, morphological or thermodynamical changes mire the interpolation and it took about 10 years to settle the "relatively simple" problem of the surface magnetism of Ni(100) [1]. Totally unclear is the magnetic coupling between the moments of atoms in systems of reduced dimensions, in particular if the frustration of the magnetic interactions comes into play as for example in exchange-bias systems.

The magnetic ground-state properties may be divided into (i) the formation of local moments of different sizes (ii) the interaction between the local moments responsible for the formation of the magnetic order, the magnetic coupling at interfaces or across spacer layers, and (iii) the magnetic anisotropy energy, which couples the direction of the magnetization to the lattice and determines the easy and hard axes of the magnetization. At this point it may be useful to put the magnetic energies involved in (i)–(iii) into a general perspective by comparing them in Table 1

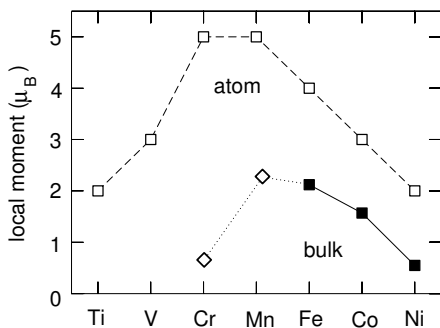


Fig. 1. Local magnetic moments of isolated $3d$ atoms (empty squares connected by dashed line), ferromagnetic (solid squares connected by solid line) and antiferromagnetic (diamonds connected by dotted line) $3d$ bulk metals. The magnetism of the atom includes only the moment due to the d electrons. For the bulk metals the experimental spin moments are shown.

Table 1: Typical ground-state energies E in eV/atom for 3d metal films

	E (eV/atom)
cohesive energy	5.5
local moment formation	1.0
alloy formation	0.5
magnetic order	0.2
structural relaxation	0.05
magnetic anisotropy	0.0001÷0.002

with the structural and compositional ground-state energies. From the relative importance of the different energies it is evident that the local moment formation has a considerable influence on the stability, alloy formation, atom arrangement and atom relaxation at the interface. Since the local moments may change quite substantially at the interface, materials with new and unknown phases [2], crystal structures and magnetic structures [3] are to be expected. Despite the technological importance and the importance for the finite temperature properties of thin films, the anisotropy energy is a rather small quantity, which is energetically nearly decoupled from the rest and is therefore treated separately in the chapter *Reduced Dimension II*. The anisotropy energy depends on all structural and electronic details of an interface, while in turn, with the exception of the magnetostriction, not much influence on structural aspects are expected. In this sense the problem of the magnetic anisotropy can be tackled after the interface is completely determined otherwise.

There are several low-dimensional systems and phenomena which are not covered in this chapter. To these belong the *Magnetic Nanoparticles*, *Magnetic Clusters* in the gas phase, the *Molecular Magnets* and the *Kondo-effect* at surfaces, which will be discussed in detail in subsequent chapters. When the growth of thin films is repeated to form multilayers, in particular those of thin magnetic films separated by non-magnetic spacer layers, an exchange interaction between the films across the spacer layer occurs, which is known as the *interlayer exchange coupling*, for which a separated chapter is devoted to. Here, we do not include the thermodynamic properties of low-dimensional systems, which are partly discussed in the chapter *Localized Moments: Finite temperature*. The work which I present here are basically predictions, analyzes and understanding of the magnetic moment and magnetic structure on the basis of the electronic structure, – results obtained from the density functional theory introduced in the chapter *Bandmagnetism II*. The experimental counterpart can be found in the chapters *Spin-Polarized Scanning Tunneling Microscopy* and *Single-Spin Detection at Surfaces*.

2 Theory and Models

In this section the reader is reminded at the theoretical concepts used to predict and analyze the results. The theories have been introduced in previous chapters. Further, simple models are discussed to rationalize the results.

Table 2: Magnetic moments M_{LSDA} in $\mu_{\text{B}}/\text{atom}$ for Fe, Co, and Ni, calculated using the local spin density approximation (LSDA) [8]. Values are compared with experimental data for the pure spin moment M_{spin} and with the total moment M_{tot} including orbital contributions.

Metal	M_{LSDA}	M_{spin}	M_{tot}
Fe	2.15	2.12	2.22
Co	1.56	1.57	1.71
Ni	0.59	0.55	0.61

2.1 Density Functional Theory: Non-collinear Magnetism

Density functional theory [4] in the local spin-density approximation (LSDA) [5, 6] or the more recent generalized gradient approximation (GGA) [7] has been the main underlying basis for the first-principles electronic structure calculations of magnetic systems in reduced dimensions. The theory has been introduced in chapter *Bandmagnetism II*. It is based on the Hohenberg-Kohn theorem that the ground state energy E of a many-body system is a unique functional of the charge density $n(\vec{r})$ and the vector-magnetization density $\vec{m}(\vec{r})$ and is minimal for the true ground state densities.

In many applications, e.g. in ferromagnetic (FM) and antiferromagnetic (AFM) solids, there is a common magnetization axis for all atoms. For these collinear cases a global z-axis can be chosen along the direction of the magnetic field. In this case, the energy and all other physical observables become functionals of the electron density and the magnitude of the magnetization density $m(\vec{r}) = |\vec{m}(\vec{r})|$ rather than $\vec{m}(\vec{r})$, or, equivalently, of the spin-up and spin-down electron densities $n_{\uparrow}(\vec{r})$ and $n_{\downarrow}(\vec{r})$. As an example we compare in Table 2 the calculated magnetic moments of the elemental bulk ferromagnets with the experimental ones.

This formalism allows also the calculation of complex magnetic structures such as in non-collinear magnetism in general or in incommensurate spiral spin-density waves (SSDW) in particular. Such magnetic structures exist in a great variety of systems. They often occur for topologically frustrated antiferromagnets (e.g. antiferromagnets on a triangular lattice or antiferromagnets in contact with ferromagnets with atomically rough interfaces as in exchange bias systems) or materials with competing exchange interactions as for example in fcc Fe, Mn. Characteristic for non-collinear magnets is a set of magnetization axes $\{\hat{e}\}$, as the magnetization axis may change from atom to atom and the minimum of the energy functional $E[n(\vec{r}), \vec{m}(\vec{r})|\{\hat{e}\}]$ determines the magnetic structure. The spin-spiral is a particular non-collinear magnetic structure with moments that are rotated by a constant angle from atom to atom along a certain direction of the crystal. It can be described by the propagation vector of the spin-spiral \vec{q} , the rotation axis (which is, in a non-relativistic approximation, not fixed with respect to the lattice) and the relative (cone-)angle ϑ between the magnetic moment and the rotation axis. The rotation angle of the magnetic moment of an atom at the position \vec{R}_i is then given by $\varphi = \vec{q} \cdot \vec{R}_i$. For a rotation around the z -axis the magnetic moment of an atom at the position \vec{R}_i is given by

$$\vec{M}_i = M(\cos(\vec{q} \cdot \vec{R}_i) \sin \vartheta, \sin(\vec{q} \cdot \vec{R}_i) \sin \vartheta, \cos \vartheta) . \quad (1)$$

The great value of this type of non-collinear calculations rests in determining from $E[n(\vec{r}), \vec{m}(\vec{r})|\{\hat{e}\}]$ or $E[n(\vec{r}), \vec{m}(\vec{r})|\{\vec{q}\}]$ the magnetic ground state as well as the exchange parameters

J_{ij} . They enter the Heisenberg model (2) giving such access to magnon spectra, spin-wave stiffness constants, magnetic phase diagrams, finite temperature properties and magnetic excitations of the system in general [9, 10].

2.2 Heisenberg Model and Beyond

To predict the magnetic ground state of a magnetic system can be a highly nontrivial problem. In cases, for example, where competing exchange interactions between neighboring atoms cannot be satisfied, the exchange interaction is frustrated which gives rise to a multitude of possible spin-structures. In the past, the magnetism of complex spin structures of itinerant magnets have been almost exclusively discussed within the framework of model Hamiltonians, e.g. the classical Heisenberg Hamiltonian introduced and motivated in chapter *Heisenberg Model–Magnetic Interaction*,

$$H_{2\text{-spin}} = - \sum_{i,j} J_{ij} \vec{S}_i \cdot \vec{S}_j. \quad (2)$$

The spins localized on the lattice sites i, j are considered as classical vectors \vec{S} , with the assumption that the spins on all lattice sites have the same magnitude S :

$$\vec{S}_i^2 = S^2, \text{ for all } i. \quad (3)$$

The exchange interaction between the spins is described by the pair interaction J_{ij} . In localized spin systems the J_{ij} can be safely restricted to the ferromagnetic ($J_1 > 0$) or antiferromagnetic ($J_1 < 0$) nearest-neighbor (n.n.) interaction, i.e. $J_{ij} = 0$ for all i, j , except for $J_{n.n.} = J_1$. Also in itinerant magnets J_1 often dominates over the rest of the further distant pairs, however, an attempt to reproduce T_C solely from J_1 produces results from limited validity. Exchange interactions beyond the classical Heisenberg model can be motivated from a perturbation expansion of the Hubbard model [11]. Expanding the Hubbard model into a spin model, replacing the spin operators by classical spin vectors, a second order perturbation expansion reproduces the classical Heisenberg model. The fourth order perturbation treatment (the third order is zero in the absence of spin-orbit interaction) yields two additional terms of different form. One is the four-spin exchange interaction (4-spin):

$$H_{4\text{-spin}} = - \sum_{ijkl} K_{ijkl} [(\vec{S}_i \vec{S}_j)(\vec{S}_k \vec{S}_l) + (\vec{S}_j \vec{S}_k)(\vec{S}_i \vec{S}_l) - (\vec{S}_i \vec{S}_k)(\vec{S}_j \vec{S}_l)].$$

The 4-spin interaction arises from the hopping of electrons over four sites, i.e. the process $1 \rightarrow 2 \rightarrow 3 \rightarrow 4 \rightarrow 1$, the other term, resulting from the hopping $1 \rightarrow 2 \rightarrow 1 \rightarrow 2 \rightarrow 1$, is the biquadratic exchange:

$$H_{\text{biquadr}} = - \sum_{ij} B_{ij} (\vec{S}_i \cdot \vec{S}_j)^2. \quad (4)$$

The exchange parameters J_{ij} , K_{ijkl} , and B_{ij} depend on the details of the electronic structure and it is known [12] that for transition-metals the sign and magnitude are rapidly varying functions of the d -band filling. In thin films, the nearest neighbor exchange constants scaled by the appropriate power of the magnetic moment, $S^4 K_1$ and $S^4 B_1$, are about one order of magnitude smaller than $S^2 J_1$, which is for example for Mn/Cu(111) about 30 meV. The higher order spin interaction have then the effect, depending on the sign and value, to lift magnetic states degenerate in the Heisenberg model.

In itinerant magnets, the electrons that are responsible for the formation of the magnetic state do participate in the formation of the Fermi-surface and hop across the lattice. Thus, it is by no means clear how far a short-ranged n.n. interaction or even how far the Heisenberg model, and models beyond that, can go in giving a sufficiently good description of the physics of itinerant magnets at surfaces and films. We believe that the combination of ab-initio calculations and the study of model Hamiltonians provides a powerful approach to investigate the magnetic structures of complex magnetic systems.

For our purpose here, the value of the Heisenberg model lies in two facts: (i) to construct a zero-temperature phase diagram of relevant spin states as function of the exchange parameters J_{ij} and (ii) that a spin-spiral state, SSDW, with a propagation vector \vec{q} in the first Brillouin zone (BZ) is a fundamental solution of the Heisenberg model for a Bravais lattice. On a Bravais lattice it is convenient to write the spin on lattice sites in terms of their discrete Fourier components $\vec{S}_{\vec{q}}$. The Heisenberg Hamiltonian can then be written in the simple form

$$H_{2\text{-spin}} = -N \sum_{\vec{q}} J(\vec{q}) \vec{S}_{\vec{q}} \cdot \vec{S}_{-\vec{q}}. \quad (5)$$

The summation is over the reciprocal lattice vectors \vec{q} and N denotes the number of lattice sites in the crystal.

$$J(\vec{q}) = \sum_{i,j} J_{i-j} e^{-iq(\vec{R}_j - \vec{R}_i)} = \sum_{\vec{0}-\vec{R}_i} J_{\vec{0}-\vec{R}_i} e^{-iq(\vec{0}-\vec{R}_i)} = J(-\vec{q}) = J(\vec{q})^* \quad (6)$$

are the Fourier transformed exchange constants and \vec{R}_i is the real-space coordinate of lattice site i . The lowest energy

$$E(\vec{Q}) = -NS^2 J(\vec{Q}) \quad (7)$$

is found for the magnetic ground state $\vec{S}_{\vec{Q}}$ of the SSDW with wavevectors $\pm\vec{Q}$ (as well as symmetry related \vec{Q} vectors) which are obtained by minimizing the energy (5) under the condition (3). The corresponding spin structure are helical spin spirals (1) for $\vartheta = 90^\circ$ and $\vec{M}_i = -g\mu_B \vec{S}_i$. For particular \vec{Q} vectors, e.g. $\vec{Q} = \pm 2\pi/a(0, 0, 1/2)$ one may find the *uudd*-state as ground state, a collinear bilayer antiferromagnetic state of ferromagnetic double layers, which couple antiferromagnetically. This state, for example, was found in calculations for regime II of fcc-Fe films on Cu(001) [13].

In three dimensions the simplest estimate of the Néel temperature of a helical spin-spiral with wave vector \vec{Q} is based on a mean-field approximation (MFA), which leads to

$$k_B T_N^{\text{MFA}} = \frac{2}{3} S^2 J(\vec{Q}), \quad (8)$$

where k_B is the Boltzmann constant, whereas an improved formula is provided by a random phase approximation [14]. In two dimensions the isotropic Heisenberg model exhibits no long range order for finite transition temperatures. Thus, in thin films the determination of the transition-temperature requires in addition the knowledge of the magnetic anisotropy constant K which scales the T_N obtained for three-dimensions by $\sim \ln(J/K)$ [15, 16]. $\vec{Q} = (0, 0, 0)$ corresponds to the ferromagnetic state, and $J(\vec{0}) = \sum_i J_{\vec{0}-\vec{R}_i}$ is an on-site exchange parameter. At surfaces and films, the exchange interaction becomes layer dependent $J_j(\vec{0}) = \sum_i J_{\vec{R}_j-\vec{R}_i}$, j is a representative site in layer j . At the surface, the number of neighbors are reduced and thus

with respect to the bulk values also J_S is reduced at the surface $j = S$. On the other hand, due to the large magnetic moments at the surface, J_{S-1} can be larger than bulk value.

\vec{Q} is typically located at high-symmetry points (lines) of the two-dimensional Brillouin zone, where the energy (T) as function of the \vec{q} -vector should have an extremum, a maximum, a minimum (or a saddle point), depending on the exchange constants J_{ij} , and the symmetry of the high-symmetry point. In principle, one cannot exclude that the minimum of the energy will be located at any arbitrary point along the high-symmetry lines, representing an incommensurate spiral spin-density wave. In practice, we perform first-principles total energy calculations $E[n(\vec{r}), \vec{m}(\vec{r})|\{\vec{q}\}]$ along the high symmetry lines to gain an overview of possible minimum energies $E(\vec{Q})$. The role of higher order spin interactions are then investigated carrying out constraint calculations of the total energy $E[n(\vec{r}), \vec{m}(\vec{r})|\{\vec{e}\}]$ for particular paths of magnetic configurations. Zero-temperature phase diagrams in the $J_{01} \cdots J_{0i}$ space are very helpful to reduce the relevant phase space of possible spin structures. This recipe had been followed in Sect. 4.1.2 and 4.2.2 to explore the magnetic ground state of thin films. The above described mapping of ab-initio calculations to spin-models relies on the assumption, that the magnetic moment does not depend on the relative difference of the magnetization axis between atoms. For itinerant systems this is not necessarily guaranteed. The change of the moment with respect to the relative quantization axis can be mapped on spin-models introducing also higher order spin interactions.

2.3 Stoner Model

In chapter *Bandmagnetism II* the Stoner criterion for ferromagnetism

$$I n(E_F) > 1 . \quad (9)$$

was derived. The Stoner criterion is an instability condition which expresses the competition between the exchange interaction in terms of the exchange integral I which drives the system into ferromagnetism for large I and the kinetic energy in terms of the DOS $n(E_F)$ at the Fermi energy E_F , which rises in the magnetic states, the more the wider the band width or the lower the density of states, respectively. A big exchange integral and a large nonmagnetic DOS at the Fermi energy favors ferromagnetism.

A Stoner criterion analogous to (9) for a system becoming instable against a frozen spinwave of wave vector \vec{q} ,

$$I \chi_{\vec{q}}(E_F) > 1 , \quad (10)$$

can be derived. Obviously the local DOS was replaced by the \vec{q} dependent susceptibility $\chi_{\vec{q}}$, a quantity which expressed in the Heisenberg model by $J(\vec{q})$. Within eq. (10), antiferromagnetism is just a special case. While the DOS at E_F is easily accessible by experiment or electronic structure calculations, the static susceptibilities $\chi_{\vec{q}}(E_F)$ are not. This motivated us to derive an approximate criterion for antiferromagnetism which makes explicit use of the local DOS.

Small magnetic moments with the same magnitude M , but possibly different directions \widehat{M}_j at different sites j , induce in linear response theory local moments \vec{M}_i at sites i

$$\vec{M}_i = \sum_j \chi_{ij}(E_F) M \widehat{M}_j . \quad (11)$$

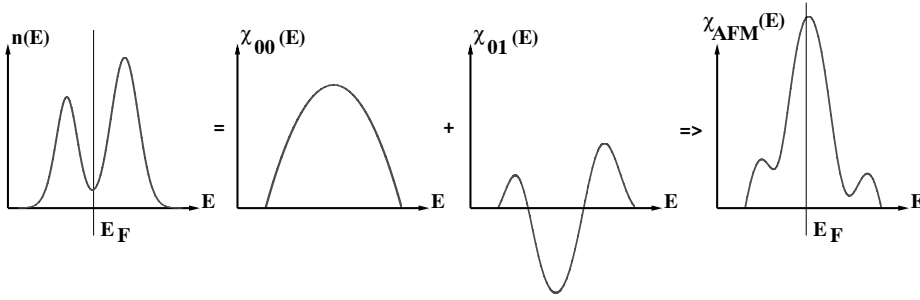


Fig. 2: Graphical illustration of (15) for a DOS typical for transition-metal monolayers on (001) oriented noble metal substrates.

The staggered susceptibility describing a particular magnetic state (M) is then expressed as

$$\chi_M = \sum_i \chi_{0i} \widehat{M}_0 \cdot \widehat{M}_i. \quad (12)$$

Particular examples of this staggered susceptibility are the ferromagnetic (χ_{FM})

$$\chi_{FM} = n = \sum_i \chi_{0i} \quad (13)$$

and the antiferromagnetic (χ_{AFM})

$$\chi_{AFM} = \sum_i (-1)^{(i)} \chi_{0i} \quad (14)$$

susceptibilities. Assuming that for $3d$ metals the nearest-neighbor interaction is the most dominating one, χ_{0i} can be neglected for all sites beyond nearest neighbors ($\chi_{0i} = 0$ for $i > 1$), and χ_{FM} and χ_{AFM} are given approximately by

$$n(E) \approx \chi_{00}(E) + \chi_{01}(E), \quad \text{and} \quad \chi_{AFM}(E) \approx \chi_{00}(E) - \chi_{01}(E), \quad (15)$$

where $\chi_{00}(E)$ is the local or atomic susceptibility, respectively, at the energy E . The energy dependence of χ_{00} is fairly simple. It follows from atomic Hund's rule-type arguments: The maximum spin M occurs for half band-filling, hence the atomic (local) susceptibility $\chi = \partial M / \partial H$ will also be largest. From (15), we can obtain an approximate form for χ_{AFM} using only DOS information. This is illustrated in Fig. 2. As function of the d band-filling, from V to Ni, the Fermi energy sweeps from the left to the right through the DOS. If the Fermi energy is positioned at the center of the band as for Cr, and the DOS is low but the antiferromagnetic susceptibility is high, and antiferromagnetism is expected. If the Fermi energy is closer to the end of the band, the antiferromagnetic susceptibility is small but the DOS is large and ferromagnetism is expected as for Fe, Co, and Ni. Mn and Fe are at the edge of both magnetic states, and depending on circumstances different magnetic ground states can be found. Compare also to calculated DOS, Fig. 13, in Sect. 4.1.1

2.4 Role of Coordination Number

As discussed in Sect. 2.3 the Stoner criterion for ferromagnetism (9) depends (i) on the Stoner parameter I and (ii) the DOS $n(E_F)$ at the Fermi energy E_F .

(i) The exchange integral I is an intra-atomic, element specific quantity, and in simplest approximation independent of the local environment, the structure and the site of a given atom, e.g. surface atom or bulk atom. According to Gunnarsson [17] and Janak [18] a global trend

$$I_{3d} > I_{4d} > I_{5d} \quad (16)$$

was found for the exchange integrals of the $3d$, $4d$, and $5d$ transition-metal series.

(ii) Focussing on the d electrons as relevant electrons for itinerant magnetism, the DOS depends on both the coordination number N_{nn} and the hopping matrix elements h_d between the d electrons. This can be understood as follows: The energy integral $\int_W n_\ell(\varepsilon) d\varepsilon = 2\ell + 1$ over the band-width W of the local DOS of angular momentum quantum number $\ell (= 2)$ is normalized to $2\ell + 1$ states. Thus, in simplest approximation possible (e.g. rectangular shaped DOS), one can assume that the local DOS scales inversely proportional to the band width W ,

$$n(E_F) \sim \frac{1}{W}. \quad (17)$$

At the atomic limit the band width converges to zero, the Stoner criterion is always fulfilled and moments in accordance with Hund's first rule will be found. In general the DOS consists of contributions from electrons in s , p , d , and f states. For transition metals by far the largest contribution comes from the d electrons, and the d - d hybridization determines the shape of the density of states. Therefore, in the following discussion we restrict ourselves to d electrons and write

$$n(E_F) \approx n_d(E_F) \sim \frac{1}{W_d}. \quad (18)$$

The average local band width $\overline{W}_d(\vec{R}_i)$ for an atom i at position \vec{R}_i can be estimated in a nearest neighbor tight-binding model, applicable for the itinerant but tightly bound d electrons of transition-metal atoms, to be

$$W_d \approx \overline{W}_d(\vec{R}_i) = 2 \sqrt{N_{nn}(\vec{R}_i)} h_d(R_{nn}). \quad (19)$$

According to (19) the band width depends on two quantities: (a) the hopping matrix element h_d of the d electrons and (b) the number of nearest neighbor atoms or coordination number N_{nn} .

(a) The hopping matrix element depends on the overlap of the d wavefunctions. It decreases with increasing lattice constant or distance R_{nn} to the nearest neighbor atom and for a given lattice constant it increases with the extension of the wavefunction or, equivalently, the number of nodes. In Fig. 3 the band widths of $3d$, $4d$, and $5d$ bulk transition-metals are schematically shown, together with the band widths of rare earths and actinides. In line with the arguments of increasing number of nodes from $3d$ to $5d$ wavefunctions a clear "macro trend" between the transition-metal series is visible summarized as follows:

$$h_{3d} < h_{4d} < h_{5d} \implies W_{3d} < W_{4d} < W_{5d} \implies n_{3d} > n_{4d} > n_{5d} \quad (20)$$

Within each transition-metal series there exists in addition a "micro trend": due to the incomplete screening of the Coulomb potential of the nucleus by the d electrons, the d wavefunctions

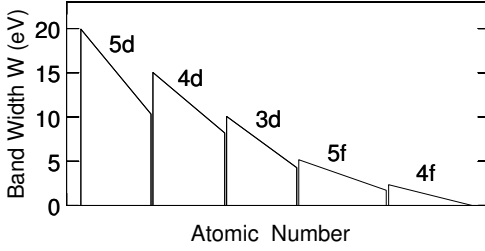


Fig. 3: Schematic illustration of the band width W of the transition–metals together with rare earths (4f) and actinides (5f), all in the bulk phase. The 5f electrons of the early actinides and the 3d electrons of transition–metals from the middle to the end of the 3d series (Cr to Ni) show itinerant magnetism, while the magnetism of the late actinides and the rare earths is best described as localized magnetism, and their magnetic properties can in good approximation be explained in terms of Hund’s rule.

at the beginning of the transition–metal series are more extent than at the end of the series, thus the hopping matrix element at the beginning of the series is larger than at the end, with the well–known consequences for the band width W and the DOS $n(E_F)$.

(b) The smaller the coordination number N_{nn} the smaller the d – d hybridization and the smaller is the band width. Let’s consider for example the coordination number of an atom in the environment of a fcc crystal ($N_{fcc} = 12$), of an atom in the (001)–surface of the fcc crystal ($N_{(001)} = 8$), and of an atom located in a two–dimensional (001) monolayer film ($N_{ML} = 4$), keeping the nearest neighbor distance fixed ($R_{nn} = \text{constant}$) and keeping the bonding strength fixed ($h_d = \text{constant}$). Under these circumstances, one obtains for the ratio of the band widths

$$W_d^{ML} : W_d^{(001)} : W_d^{fcc} = 0.58 : 0.82 : 1 ,$$

or the local DOS

$$n_d^{ML} : n_d^{(001)} : n_d^{fcc} = 1.73 : 1.22 : 1 . \quad (21)$$

The important message of (21) is, that the reduction of the coordination number leads to less d – d hybridization, thus to band narrowing, and the tendency towards magnetism is considerably increased. The reduction of the coordination number is hence responsible for the fact that the magnetism is enhanced at surfaces as compared to bulk, and the magnetism of ultrathin films should be larger than at surfaces. Accordingly, one can expect, that transition–metals, which are nonmagnetic as bulk metals, may become magnetic at surfaces or as ultra–thin films. A nice manifestation of these arguments was recently reported for the size and shape dependence of the local magnetic moments in Fe clusters on the Ni(100) [19] summarized in Section 5.2. The arguments put forward here for the increased ferromagnetism in reduced dimensions can be carried over directly to the increased antiferromagnetic susceptibility.

The magnetic properties are expected to depend also on the surface or film orientation, because along with a change of the surface orientation goes a change of the coordination number N_{nn} (cf. Table 3) as well as a change of the nearest neighbor distance R_{\parallel} between the surface atoms and R_{\perp} between the surface atoms and the atoms in the next layer. For a fcc lattice, the (111) surface is the most densely packed one, and we expect for it the smallest enhancement of the magnetic moments. Among the three low-index surfaces, with the orientation (001), (011), and (111), the (011) surface leads to the most open surface. For the latter we expect the largest

Table 3: Coordination number N_{nm} , interlayer distance d , point symmetry S , and packing density (fraction of the area of the surface unit cell, covered by atoms with an atom radius of touching bulk atoms) for a fcc lattice. Only the 3 low-index surfaces, (001), (011), and (111), are considered. a is the lattice parameter of the simple cubic unit cell.

	N_{nm}	S	d/a	ρ
(111)	9	C_{3v}	0.5774	0.9068
(001)	8	C_{4v}	0.5000	0.7854
(011)	7	C_{2v}	0.3536	0.5554

magnetic moments. At surfaces or ultrathin films of bcc lattice type the trend should be exactly the opposite. The most densely packed surface is the (011) surface for which we expected the smallest enhancements of the magnetic moments. The (111) surface is the most open one. This surface is already close to a stepped one.

The implication of the coordination number, discussed so far is an important aspect in interface magnetism, but it is not the whole story. Further important aspects neglected so far have to be taken into account in order to give a qualitative correct description of the magnetism at interfaces.

POINT SYMMETRY: The disruption of the translational symmetry due to a given interface reduces in general the point symmetry. Degeneracies typical for cubic bulk metals may be lifted. One example is the 3 fold degenerate t_{2g} bulk state, which is split at a (001) surface into a 2 fold degenerate state and a single state. This symmetry break induces a splitting or broadening of the DOS and makes magnetism unfavorable. A famous victim of this scenario is Pd. Bulk Pd has a large density of states at the Fermi energy which contributes to a large exchange enhanced susceptibility. Thus bulk Pd is nearly ferromagnetic. The band narrowing experienced at the surface due to the reduction of the coordination number should drive the surface of Pd into the ferromagnetic state. But this is not the case. Instead, the change of the surface symmetry splits the states at the Fermi energy, broadens the DOS and counteracts the band narrowing. The surface of Pd(001) remains nonmagnetic.

SHIFT OF THE d BAND RELATIVE TO THE sp BAND: Compared to a single isolated atom, the d electrons in a solid are in a state of compression. Therefore, in a solid their energy levels are positioned at a much higher energy than in an atom. At the surface the charge density of the d electrons can relax and their energy levels move downwards. They are situated closer to the bottom of the sp band and the number of d electrons is increased or the d holes are decreased. This downward shift is often facilitated by a significant hybridization of the d electrons with sp electrons or holes e.g. of the substrate. As depicted in Fig.4 this leads to an Lorentzian tail of the DOS. If this tail is positioned close to the Fermi energy, magnetism can be drastically reduced as for example for a single Ni monolayer on Cu(100), for which the local Ni moment amounts to $0.33 \mu_B$ as compared to the magnetic Ni moment at the Ni(100) surface ($0.72 \mu_B$). For a monolayer Pd on Ag(100) magnetism is even absent. In both cases we would expect an increase of the moment due to the reduction of the coordination number by a factor two when compared the respective (100) surface. On the other hand elements at the beginning of the transition-metal series such as V profit from this effect and magnetism can appear more likely.

$sp-d$ DEHYBRIDIZATION: The main carrier of itinerant magnetism are the d electrons. For atoms, we know, the number of d electrons are integer numbers. In metallic systems, this is

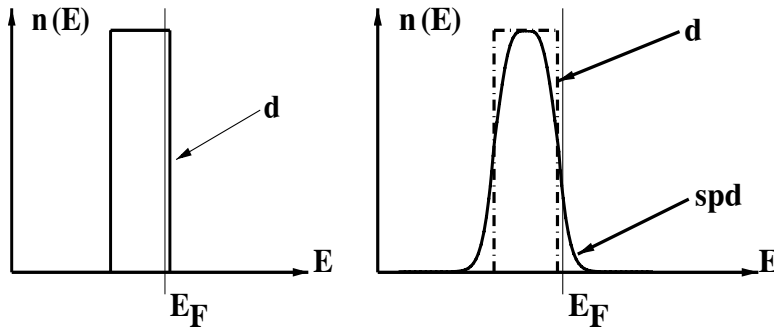


Fig. 4: Schematic illustration of the hybridization of the overlayer d electrons with the sp electrons e.g. of the substrate, on the density of states, (left) without (right) with hybridization.

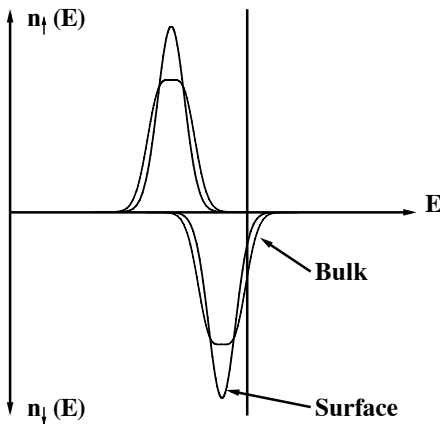


Fig. 5. Schematic illustration of the role of the sp - d dehybridization on the density of states of the d electrons $n_d(E)$. The integrated density of d states for the surface is larger than for the bulk.

not the case, the number of d electrons is a fractal number and depends, besides the dominating $d-d$ hybridization, on the hybridization with the s and p electrons. Due to the hybridization of the d electrons with the sp electrons, d states below the Fermi energy are hybridized into unoccupied sp hybrids and the number of d electrons is reduced when compared to the isolated atom. This so-called sp - d dehybridization changes as function of the coordination number or the nearest neighbor distance the fractional number of d electrons without any topological change of the DOS. This is illustrated in Fig. 5. Surfaces and monolayers with their smaller coordination numbers have therefore a higher number of d electrons favorable for magnetism. For an illustration, in a computer experiment we investigated the magnetic moment of one layer of Ni for various lattice parameters and coordination numbers. In Table 4 one finds that with decreasing coordination number and with increasing atom separation the magnetic moment increases although the Ni majority band is always completely filled.

CHARGE NEUTRALITY: The local charge neutrality has to be fulfilled in order to avoid the otherwise appearing strong Coulomb forces. It induces again a band alignment. Band narrowing (at interfaces) means automatically that the number of electrons must change. To avoid charged interfaces a realignment of the center of gravity of the bands occurs. The d band, which moved to lower energy in order to relax the compression moves now upwards again. Due to an upward

Table 4: Calculated magnetic moments in units of μ_B for Ni(001) as an unsupported, free-standing monolayer (coordination number $N_{nn} = 4$), as a function of the lattice constant: $a_{Ag} = 7.79$ a.u., $a_{Pd} = 7.42$ a.u., $a_{Cu} = 6.76$ a.u., and $a_{Ni} = 6.65$ a.u.. $N_{nn} = 8$ indicates the local magnetic moment of the Ni(001) surface and $N_{nn} = 12$ indicates the bulk value. Included is also the local magnetic moment of the Ni(011) surface ($N_{nn} = 7$).

N_{nn}	lattice parameter			
	Ag	Pd	Cu	Ni
4	1.02	0.96	0.87	0.85
7	–	–	–	0.74
8	–	–	–	0.72
12	–	–	–	0.59

shift in the energy, the minority and majority electrons become depopulated differently and together with the change of the number of majority electrons due to the $sp-d$ dehybridization the magnetic moment increases. All together we find a complex alignment of all the bands individually for each symmetry of the electrons.

STRONG AND WEAK FERROMAGNETS: Despite the drastic change of the coordination number and the lattice parameter, the Ni moment in Table 4 changes only in the range of $\pm 20\%$. This is typical for strong ferromagnets (magnets with filled majority band). In general, one can say that the magnetism of strong ferromagnets is rather robust against any environmental changes. Weak ferromagnets (magnets with partly occupied majority bands) are sensitive to any environmental changes with moments collapsing easily.

Neglecting these interwoven effects has caused in the past confusion in the field of surface and interface magnetism. They are readily included by performing self-consistent first-principles calculations.

3 Surfaces

3.1 General Overview

The theoretical studies of the magnetism of the transition-metal surfaces can be summarized as following: Magnetic moments have been found for all investigated surfaces of Cr, Fe, fcc and hcp Co, and Ni. The surface of Mn has not been investigated seriously, due to the many possible bulk ground states. The surface magnetism of V(100) and Rh(100) is still controversial. For both surfaces there are experimental [20, 21, 22] and theoretical [23, 24, 25, 26, 27] investigations suggesting surface magnetism, while we and others concluded that the V(100) [28, 29, 30] and Rh(100) [31] surfaces are nonmagnetic. Probably Rh(100) is at the edge of becoming magnetic. For the (100) surface of the Pd, which exhibits a strong Stoner enhanced susceptibility in bulk, no surface magnetism was found. Although bulk V, Ru, Rh, and Pd metals are nonmagnetic, the M_xV_{1-x} alloys with $M=Ru, Rh, Pd$ are nonmagnetic, and the (100) surfaces of V, Ru, (Rh,) and Pd are also nonmagnetic, Turek *et al.* [32] showed that the (100) surfaces of the M_xV_{1-x} alloys are magnetic. In Table 5 the calculated local magnetic spin moments of the

Table 5: Calculated local magnetic spin moments $M_S^{(100)}$, $M_S^{(110)}$, and $M_S^{(111)}$ in comparison to the corresponding magnetic bulk moments M_B in μ_B/atom for bcc Cr, Fe, fcc Co(100), hcp Co(0001), and fcc Ni.

	Cr	Fe	Co	Ni
$M_S^{(100)}$	2.55	2.88	1.85	0.68
$M_S^{(110)}$	–	2.43	–	0.74
$M_S^{(111)/(0001)}$	–	2.48	1.70	0.63
M_B	± 0.60	2.13	1.62	0.61

(100), some (110) and (111) surfaces are collected together with the corresponding bulk values for comparison. For all magnetic metals the magnetic surface moments exceed the bulk values. With respect to the bulk values for Cr(100) and Fe(100) the calculated surface moments are enhanced by a factor 4.25 and 1.35, respectively. The enhancement of the calculated moments at the Co and Ni surfaces is relatively small. Co and Ni are strong ferromagnets and the enhancement is basically due to a $sp-d$ dehybridization, while Cr and Fe are weak (anti)ferromagnets which can occupy additional majority d states on the dispense of minority d states. In agreement with our understanding of the relation between the surface coordination number and the magnetic moment of fcc and bcc metals, the magnetic moment of a Ni atom at the Ni(110) surface is larger than for a Ni atom at the Ni(100) surface. The smallest moment is found at the close-packed Ni(111) surface. For bcc Fe it is slightly different: Also here the smallest moment is found at the close-packed (110) surface. The largest moment, however, was not found for the most open Fe(111) surface, but for the (100) surface. Both the (100) and the (111) surface have four atoms with nearest neighbor bulk distance, but differ in the number of next-nearest neighbor atoms and their distribution in surface and subsurface layer.

In general the screening of the surface due to the d electrons is rather efficient. The surface induced perturbation of the magnetic moments does not penetrate deeply into the bulk. The moments at the fcc Co(100) or hcp Co(0001) surfaces reach already the bulk value in the first, latest in the second layer below the surface. For bcc (100)–surfaces, as e.g. Fe or Cr the perturbation penetrates a bit deeper into the bulk. This is understood by the fact that for these surfaces the change of the surface moments (or perturbation) is larger. Additionally for bcc metals with half d band filling the bcc-pseudogap in the density of states provides a worse screening of the surface perturbation and surface states can penetrate deeper into the bulk. For comparison we present in Fig. 6 the layer resolved magnetic moments for Fe(100) and Fe(110).

3.2 Example: Cr(100)

Both, V and Cr are bcc $3d$ transition metals with about half-band filling. From band theory we expect antiferromagnetism along the [001] direction which will convert at the (100) surfaces to ferromagnetic (100) planes which couple antiferromagnetically from layer to layer, which is called layered antiferromagnetism (LAF) (see Fig. 7). More accurately the ground state of bulk Cr is a spin-density wave (SDW) state where the LAF structure is modulated by a wave vector $\vec{q}_0 = 2\pi/a_0(0, 0, q_0)$; $q_0 = 0.952 \approx 19/20$. The SDW in bulk Cr can be ascribed to the so-called nesting between parallel sheets of the paramagnetic Fermi surface [34], which

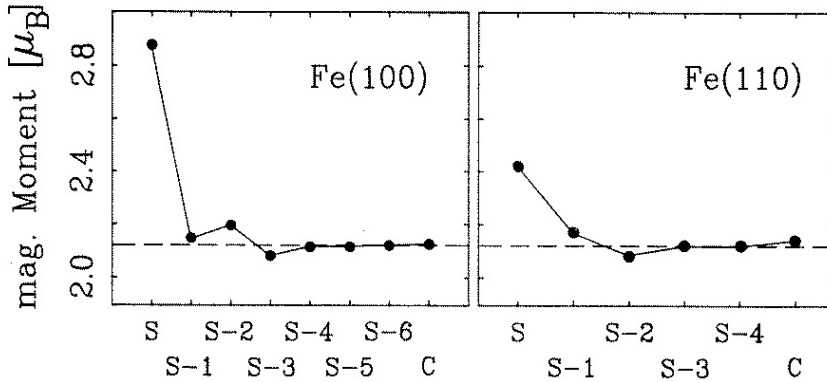


Fig. 6: Layer resolved local magnetic Fe moment from the surface (S) to the bulk (C) for Fe(100) and Fe(110) [33].

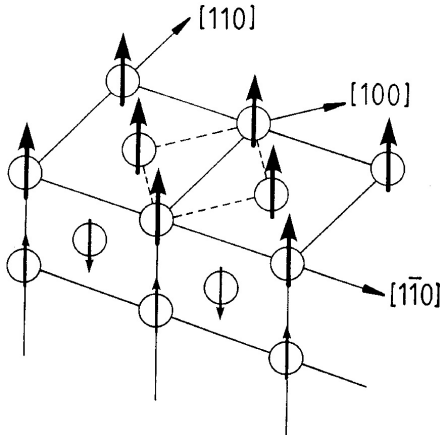


Fig. 7. The layered antiferromagnetic structure. Spins are depicted perpendicularly to the surface only for graphical simplicity. The surface $p(1 \times 1)$ unit cell is given by dashed lines. Bulk moments are presented by shorter arrows than surface moments to signify their different size.

gives rise to a peak in the \vec{q} -dependent spin susceptibility $\chi(\vec{q})$ at the nesting wave vector \vec{q}_0 . The surface breaks the symmetry, thus the Fermi surface topology alters and the nesting feature may disappear. Therefore, one can envisage that no SDW appears in the vicinity of the surface or interface. This problem has been investigated recently by the Uppsala group for Fe/Cr [35] and Cr/Mo [36] films, and by Bihlmayer *et al.* [30] for Cr(100). At first GGA calculations of the Cr(100) surface in the LAF state were carried out. This surface exhibits a magnetic moment of $2.6 \mu_B$ that decays rapidly to the bulk value (see right of Fig. 8). Then a compressed (corresponding to $q = 11/12$) SDW is introduced in a 23-layer Cr film terminated by two Cr(100) surfaces. In the left of Fig. 8 we see an anti-node located at the surface which has a moment of $2.4 \mu_B$, while the magnetic moment in the center of the film indicated as C in Fig. 8 are similar to the bulk values of bulk Cr with a SDW of $q = 11/12$. This film-SDW is a (meta)stable magnetic configuration since it is 12.7 meV higher in energy than the LAF state, but it is a stable solution. From a certain film thickness on the SDW should then be lower in energy than the LAF state. These energy differences, though, have to be taken with some care. LSDA and GGA calculations seem to predict a somewhat too strongly enhanced

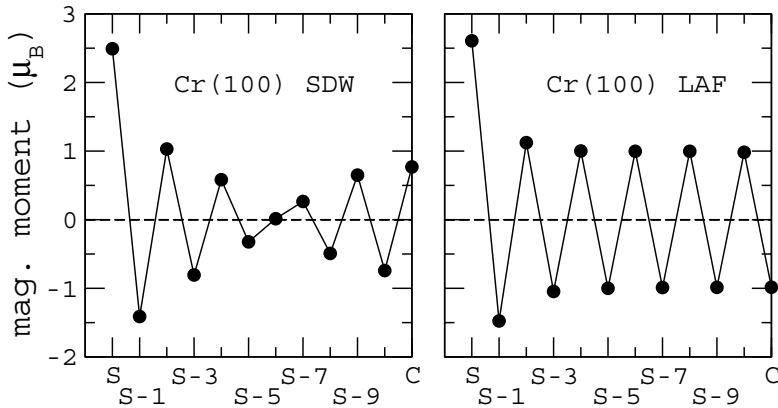


Fig. 8: Layer resolved local magnetic Cr moments from the surface (S) to the bulk (C) for the Cr(100) surface [30]. Left figure includes a stable bulk spin-density wave (SDW) with a node at atom S-6, right figure for layered antiferromagnetic (LAF) Cr. Calculations were carried out in a film geometry of 23 layers. Bulk value was reached in the center layer indicated by C.

magnetic surface moment of $2.5 \mu_B$ and $2.6 \mu_B$, respectively. Surface relaxation reduced the GGA surface moment from $2.61 \mu_B$ to $2.45 \mu_B$. Reducing this value artificially to $1.75 \mu_B$, brought a reasonable agreement with tunneling spectroscopy measurements of the spin-split d_{z^2} surface state of Cr(100) [37]. Currently it is not clear whether this is an error of the LSDA or GGA or due to finite temperature. This inaccuracy in the theoretical determination of the magnetic bulk and surface moments may translate in an inaccurate estimate of the critical Cr film thickness from which on the SDW becomes more stable than the LAF solution.

To study the influence of the surface moment on the SDW, a Cr(100) surface capped with one monolayer of V was calculated. V and Cr have similar lattice constants and thus it should be experimentally possible. We find that V couples layered antiferromagnetically to Cr. The surface moment of V is $2.1 \mu_B$ and surprisingly the Cr moment at the V/Cr interface is reduced to $0.6 \mu_B$. In this case, Cr forms the onset of a node at the interface. Introducing a SDW in this system leads to an unstable magnetic arrangement that decays into the LAF state, which is energetically very close. The actual results depend sensitively on the interlayer relaxation. The interlayer relaxation of the V/Cr interface reduces the V moment to about $1.3 \mu_B$ and the Cr moment increases about $0.7 \mu_B$.

The experimental verification of the surface magnetism of a LAF system such as the Cr(100)

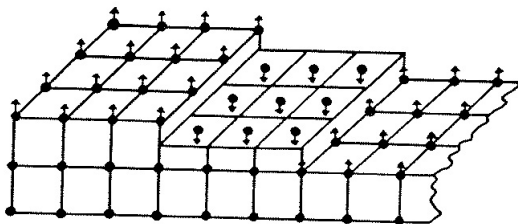


Fig. 9. Topological antiferromagnetic order of a Cr(100) surface with terraces separated by single surface steps. Different terraces are magnetized in opposite directions. Only surface spins are indicated. Spins are depicted perpendicularly to the surface only for graphical simplicity.

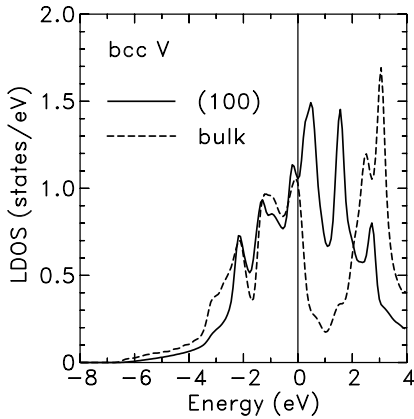


Fig. 10. Local density of states per spin for a non-magnetic V atom located in bulk V and at the V(100) surface.

surface turned out to be rather difficult. Any realistic surface consists of terraces of at most $1 \mu\text{m}$ in width separated by mono-atomic steps. From terrace to terrace the surface magnetization may flip and in average the magnetization of the surface cancels between oppositely magnetized terraces. Obviously terraces introduce a new length scale which lead to *topological antiferromagnetism* depicted in Fig. 9 on a sub-micrometer scale. Recently this picture was confirmed experimentally by spinpolarized scanning tunneling spectroscopy [38].

3.3 Example: V(100)

We investigated the possible magnetism of the V(100) surface using a 15 V layers thick film terminated by two V(100) surfaces. For a structurally unrelaxed 15 layer V film the surface magnetic moment was only $0.15 \mu_B$ and the magnetic moment of the subsurface layer was already as small as $-0.06 \mu_B$. The introduction of the surface relaxation ($\Delta d_{12} = -11.1\%$, $\Delta d_{23} = +0.7\%$, $\Delta d_{34} = +3.1\%$ of the bulk interlayer distance) by total energy minimization finally quenched the magnetism completely. The same happened for a V(105) step-edge, ferromagnetism of the step-edge disappeared after relaxation. In an older LSDA investigation, we studied the magnetism of (unrelaxed) 1, 3, and 5 layers V films in a $c2 \times 2$ unit cell, i.e. with two atoms per film plane (see Sect. 4.1.2). While the unsupported monolayer was clearly in-plane antiferromagnetic, the trilayer system was on the edge of a magnetic stability, while the 5 layer system was always nonmagnetic. From these results we conclude that in very thin V films a surface magnetic moment can be stabilized, while for thicker and relaxed films no surface magnetism can be found. In Fig. 10 the local density of states of a V atom at the (100) surface and in bulk are presented. We see that both have roughly the same density of states $n(E_F)$ at the Fermi energy. According to the Stoner criterion, $In(E_F) > 1$, the surface magnetism of V is not more likely than the magnetism of bulk V.

3.4 The (100)-Surfaces of VRu, VRh and VPd Alloys

Common to all bcc (100)-surfaces is a d_{z^2} surface state located in the pseudogap of the density of states of the bcc metals separating bonding from antibonding states. For Cr, Mn and Fe this surface state is spin-split and attracted recently a wide attention as it was used to probe

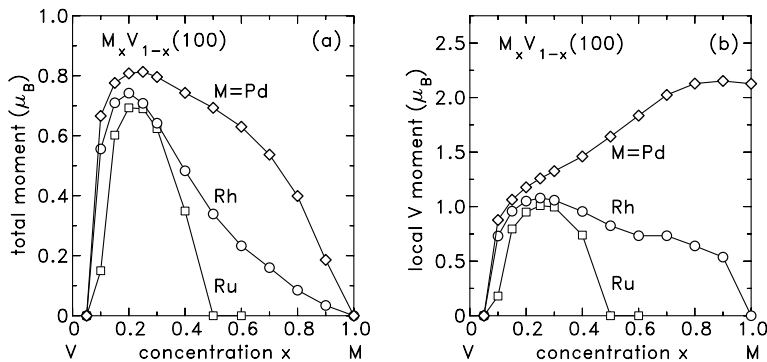


Fig. 11: (a) shows the total magnetic moment of the semi-infinite (100) Ru_xV_{1-x} , Rh_xV_{1-x} , and Pd_xV_{1-x} alloy as function of the 4d transition-metal concentration x . (b) shows the local V magnetic moment of a V atom located in the surface layer of the (100) surface of these alloys.

and image the surface magnetism of these systems using (spin-polarized) scanning tunneling microscopy and spectroscopy. One example is the observation of the topological antiferromagnetism of Cr(100) discussed above. This surface state is clearly visible as a strong peak in the LDOS of Fig. 10, a few tenths of an eV above E_F . Magnetism could be possible by extending this peak to the vicinity of the Fermi energy. This is achieved by alloying V, for example, with Ru, Rh, or Pd. The main effect of alloying is to broaden this peak due to the scattering of electrons in the random alloy. Turek *et al.* [32] have explored this idea and found that all three systems exhibit magnetism over a wide range of concentrations which is unexpected taking into account that all those bulk alloys are nonmagnetic and that V, Ru, Rh, and Pd are nonmagnetic in the bulk and at the surface. The magnetic moment as function of the concentration are summarized in Fig. 11. The largest total moments of $0.7\mu_B$, $0.75\mu_B$, $0.8\mu_B$ were found for $Ru_{0.2}V_{0.8}(100)$, $Rh_{0.2}V_{0.8}(100)$, and $Pd_{0.25}V_{0.75}(100)$. A closer analysis reveals that the primary contribution to the magnetism is due to the large local moments of V in the surface layer. These are shown in Fig. 11b. For RuV and RhV we find peak V moments of about $1\mu_B$ at about 25% Ru or Rh concentration.

From the investigation of the surface magnetism, in particular the investigation of the layer dependence of the local moments from the surface to the bulk, we can draw the very important conclusion that at perfect surfaces the changes of the local moment due to the existence of a surface is limited in first approximation to the atoms in the surface layer. A better description may include the changes of the moments in about the first 4 layers at the surface. In the context of thin films this observation means that the new properties different from the surfaces are only expected in the ultrathin limit of films such as monolayers, bilayers up to a few layers.

4 Ultrathin Films

The transition-metal monolayers on noble-metal substrates are the classical systems exhibiting two-dimensional (2D) magnetism. Because of the reduced coordination number of nearest neighbor transition-metal atoms in a monolayer film, the d -band width in two-dimensions is considerably smaller and correspondingly the LDOS at the Fermi energy is considerably larger

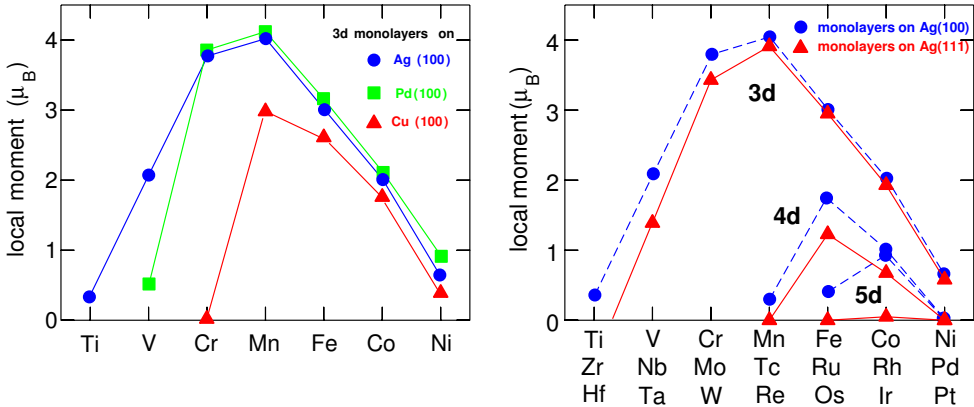


Fig. 12: Local magnetic moments as calculated for ferromagnetic (left figure) 3d metal monolayers on Ag(100) [39] (dots), Pd(100) [40] (squares), and Cu(001) [2] (triangles), and (right figure) 3d, 4d [45], and 5d [46] monolayers on Ag(001) (dots) and Ag(111) [44] (triangles).

than in the bulk situation. Thus the magnetic instability should occur for a much wider variety of transition-metal elements. Following this line of argument it is clear that the strength of the d - d hybridization between monolayer and substrate is an additional parameter which controls the d -band width of the monolayer. For instance, large band-gap material, e.g. MgO(100), as substrate allows the formation of two-dimensional monolayer bands within the band gap of the substrate material. In this case the impact on the magnetization of the monolayer due to the substrate is expected to be small. The same is true for noble-metal substrates, which have d bands well below the Fermi energy. The width of the monolayer d band is not significantly broadened by the monolayer-substrate d - d interaction, and magnetism is restricted to the monolayer. Increasing the d - d hybridization by choosing appropriate nonmagnetic transition-metal substrates, e.g. Pd(100) or W(110), will lead to a considerable broadening of the monolayer bands and introduce a significant spin-polarization of the substrate until we have changed from the two-dimensional limit to the semi-infinite regime. Choosing a magnetic substrate an additional complexity arises due to the competition of the magnetic coupling in the monolayer and between monolayer and substrate.

4.1 (100) Oriented Monolayers on Nonmagnetic Substrates

4.1.1 Ferromagnetic Monolayers

A systematic investigation of the magnetism of all possible 3d, 4d, and 5d transition-metals monolayers on Ag(001) are collected in Fig. 12 and in Table 6. One finds that all 3d metal monolayers (Ti, V, Cr, Mn, Fe, Co, Ni) on Ag(001) substrate show ferromagnetic solutions. Tc, Ru, and Rh are ferromagnetic among the 4d-metals, and Os and Ir are ferromagnetic among the 5d-metals on Ag(001). The local magnetic moments are partly very large, not only for the 3d monolayers, but surprisingly also for the 4d and 5d ones. In the 3d series the overall trend of the local moments follows Hund's first rule. The largest local moment of about $4 \mu_B$ was found for Mn and from Mn to Ni the magnetic moment decreases in steps of $1 \mu_B$. The latter is a consequence of the strong ferromagnetism in these monolayers. The magnetic moments of

Table 6: Local magnetic moments in μ_B/atom for 3d transition-metal atoms as ferromagnetic (F) and antiferromagnetic (AF) 3d monolayers (ML) on Ag(001) [39], Pd(001) [40], W(110) [41] and on Cu(001) [2, 42]; compared with results for 3d monolayers as interlayers (IL) in Cu(001) [2], unsupported (001) monolayers (UL) in the lattice constant of Cu(111) and Ag(001) [43], and with results for ferromagnetic 3d monolayers on Cu(111) and Ag(111) [44]. “–” indicates that no calculation was performed for this system. “0” indicates that the calculated moment was smaller than the numerical accuracy estimated to be about $0.02 \mu_B/\text{atom}$. “?” indicates a system, for which the calculation was not finished up completely to self-consistency, but result is approximately correct.

				Ti	V	Cr	Mn	Fe	Co	Ni
Ag	ML	on Ag(001)	F	0.34	2.09	3.78	4.04	3.01	2.03	0.65
			AF	0	2.08	3.57	4.11	3.06	?	0
	UL	– Ag(001)	F	1.72	2.87	4.50	4.32	3.29	2.20	1.02
			AF	0	2.59	4.09	4.32	3.32	2.10	0
	ML	on Ag(111)	F	0	1.39	3.43	3.91	2.95	1.93	0.51
	Pd	ML	on Pd(001)	F	0	0.51	3.87	4.11	3.19	2.12
AF				0	1.39	3.46	4.05	3.20	1.99	0.59
W	ML	on W(001)	F	–	0.00	–	2.97	2.37	1.14	0.00
			AF	–	0.00	2.52	3.32	–	–	0.00
Cu	ML	on Cu(001)	F	–	0	0	2.97	2.61	1.76	0.33
			AF	–	0	2.52	2.92	2.35	?	0
	IL	in Cu(001)	F	–	0	0	2.01	2.39	1.51	0
			AF	–	0	1.84	2.15	–	–	–
	ML	on Cu(111)	F	–	0	0	3.05	2.69	–	–
	UL	– Cu(111)	F	–	0	0	3.06	2.75	–	–

Ti, V, and Cr monolayers show a pronounced dependence on the substrate: Ti is magnetic on Ag, but nonmagnetic on Pd; the magnetic moment of V is reduced by more than $1.5 \mu_B$ when changing the substrate from Ag to Pd; and for Cr the magnetic moment changes from $3.8 \mu_B$ as an adlayer on Ag or Pd to zero as an adlayer on Cu. Although not as dramatic, the reduction is also visible for Mn. We attribute the drastic reductions of the monolayer moments to the reduction of the lattice constants in the sequence Ag to Pd to Cu.

When comparing the results of the local moments between 3d, 4d, and 5d monolayers on Ag(001) an interesting trend is observed: The element with the largest magnetic moment among each transition metal series is shifted from Mn to Ru (isoelectronic to Fe) and at last to Ir (isoelectronic to Co), respectively. Following these trends we do not expect ferromagnetism for any other 4d or 5d metal on noble metal (001) substrates, and indeed Mo and Re remained nonmagnetic. The overall picture of monolayers on Ag and Au is the same, but the different substrate interactions cause Tc and Os on Au to be nonmagnetic and lead to a slightly larger moment for Rh. Pd and Pt are predicted to be nonmagnetic. With the exception of Ru, for which a rather small magnetic moment of $0.2 \mu_B$ was calculated, no monolayer magnetism was found for 4d metals on Pd(100). Investigations [47] including the spin-orbit interaction have shown

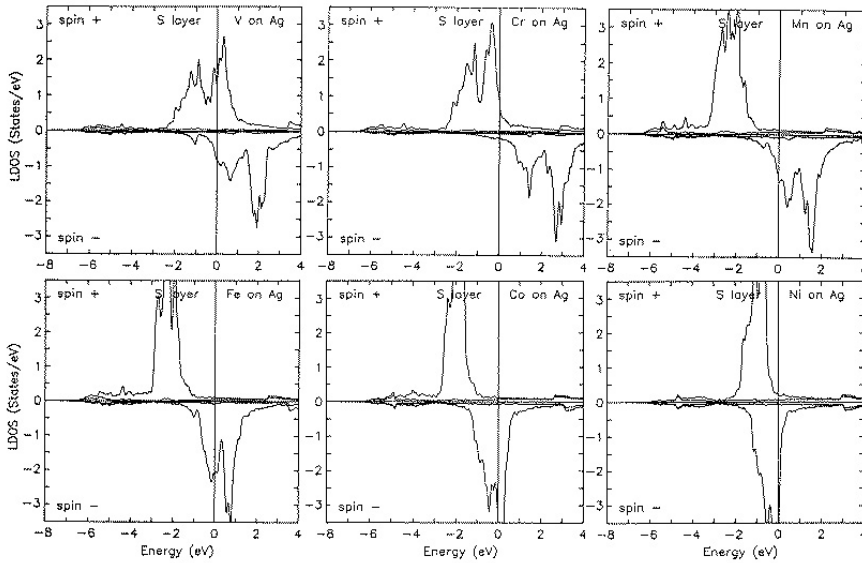


Fig. 13: Local density of states (LDOS) of ferromagnetic 3d metal monolayers on Ag(100). The Fermi energy defines the origin of the energy scale, separating occupied (at negative energies) from unoccupied states (at positive energies). Majority (minority) states are indicated by positive (negative) values of LDOS.

that the spin-orbit interactions reduces significantly the magnetic spin moment of the 5d metal monolayers and depending on the interlayer relaxation the spin moment might be suppressed.

4.1.2 Antiferromagnetic Monolayers

It is by no means clear whether the ferromagnetic state is actually the magnetic ground state. Looking at the LDOS of the 3d monolayers in Fig. 13 and considering the analysis of the antiferromagnetic susceptibility (15) we expect an antiferromagnetic phase for Cr and possibly also for V and Mn monolayers. In reality, various antiferromagnetic states as well as non-collinear spin configurations could be anticipated. Studying an Heisenberg model (2) for a square lattice as formed by the (001) monolayers up to the second nearest-neighbor interaction (J_1 , J_2) the situation becomes relatively simple. As long as the nearest-neighbor interaction is the dominating one, there are only two phases to be considered: the ferromagnetic $p(1 \times 1)$ structure ($J_1 > 0$) discussed in the previous section and the antiferromagnetic $c(2 \times 2)$ superstructure ($J_1 < 0$, a checkerboard arrangement of up and down spins similar to the $c(2 \times 2)$ ferrimagnetic structure in Fig. 20, but with moments of identical size on both sub-lattices). The $c(2 \times 2)$ structure corresponds to the \bar{M} -point in the 2DBZ of the square lattice. If the next-nearest neighbor interaction is antiferromagnetic, $J_2 < 0$, and sufficiently strong, $|J_1| < 2|J_2|$, then the magnetic structure with a 2D \vec{Q}_{\parallel} vector of the \bar{X} -point in the 2DBZ, corresponding an antiferromagnetic $p(2 \times 1)$ or $p(1 \times 2)$ structure (ferromagnetic rows of atoms along the [100] or [010] direction coupling antiferromagnetically from row to row) becomes the magnetic ground state.

Figure 14 shows the local moments for the ferromagnetic and $c(2 \times 2)$ antiferromagnetic phase

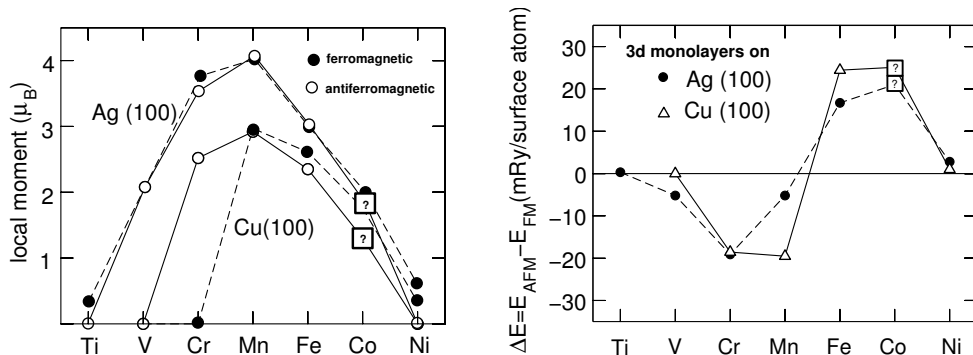


Fig. 14: Left figure: Local magnetic moments of 3d monolayers on Cu(100) [2] and Ag(100) [39] calculated for the $p(1 \times 1)$ ferro- (solid circles connected by dashed line) and the $c(2 \times 2)$ antiferromagnetic configuration (open circles connected by solid line). Right figure: Total energy difference $\Delta E = E_{AFM} - E_{FM}$ per 3d atom between the $c(2 \times 2)$ antiferromagnetic and $p(1 \times 1)$ ferromagnetic phase for 3d monolayers on Cu(100) (triangle connected by full line) and Ag(001) (solid circles connected by dashed line). $\Delta E > 0$ (< 0) means, the ferromagnetic (antiferromagnetic) configuration is the most stable one. “?” indicates an result which is not fully converged.

of 3d monolayers on Cu(001). It becomes evident that, for many systems (see also Table 6) both configurations exist with moments of similar values. Depending on the inplane lattice constant, differences in the local moments for the two magnetic phases develop for earlier transition metals, e.g. for Cr on Cu(001), for V on Pd(001) or for Ti on Ag(001). Figure 14 shows also the energy differences $\Delta E = E_{AFM} - E_{FM}$ per atom between the $c(2 \times 2)$ antiferromagnetic and the ferromagnetic configuration for 3d metal monolayers on Cu(001) and Ag(001). A clear trend emerges: The Ni, Co, and Fe overlayers ($\Delta E > 0$) prefer the ferromagnetic configuration and the Mn, Cr, and V ones favor the antiferromagnetic one. From the strong similarities of the monolayer trends for these two substrates we conclude, that this is a general trend: Fe, Co, and Ni favor the $p(1 \times 1)$ ferromagnetism on the (001) surfaces of Pd, Pt and the noble metals Cu, Ag and Au [48] whereas V, Cr, and Mn monolayers prefer the $c(2 \times 2)$ antiferromagnetic configuration. The same trend was recently found for monolayers on W(110) [41], and is expected for Al substrates although V and Ni might then be nonmagnetic. Since $\Delta E \approx 8S^2J_1$, ΔE reflects basically the change of J_1 as function of the band filling (number of d electrons) or how E_F moves through the LDOS in Fig. 13. For Mn on Ag(001), where ΔE or J_1 , respectively, is relatively small, the J 's between more distant pairs may determine the picture. We investigated by total energy calculations the stability of the possible $p(2 \times 1)$ structure and found that the $c(2 \times 2)$ structure is indeed the magnetic ground state.

The $c(2 \times 2)$ antiferromagnetic phase was first predicted by theory. After the prediction several experiments indicated that the $c(2 \times 2)$ state may indeed exist: no ferromagnetic long range order was found at low temperatures for a V monolayer on Ag(100) [49], but a local exchange splitting was found for V, Cr, and Mn monolayers on Ag(100) [50]. More than 10 years after the theoretical prediction a direct proof of the $c(2 \times 2)$ antiferromagnetic state became for the first time possible by using the spin-polarized scanning tunneling microscopy in the constant-current mode [51, 52]. The experiments were carried out for a Mn monolayer on W(110).

4.1.3 Magneto-Interlayer Relaxation

In order to give the reader an impression (i) how strongly the formation of large monolayer moments may affect the interlayer relaxation and (ii) what is the influence of the magnetic order on the interlayer distance, total energy calculations as function of the interlayer distances are presented for two selected systems: Mn/Ag(001), and Mn/Cu(001). Prior to these calculations we determined the in-plane lattice constants which are taken to be the bulk lattice constants of the substrate; we found a value of $a_0^{\text{Cu}} = 6.65$ a.u. for Cu and $a_0^{\text{Ag}} = 7.58$ a.u. for Ag. Clearly, the Mn monolayers show the largest magnetic moments on any substrate and the magneto-volume effects should be most substantial.

Fig. 15 shows the total energy as function of the interlayer distance for a Mn monolayer on Cu(001) and Ag(100) for three different magnetic states: nonmagnetic, ferromagnetic and $c(2 \times 2)$ antiferromagnetic. We find, as already discussed in Sect. 4.1.2 that the nonmagnetic solution is the highest in energy and the antiferromagnetic one is the lowest energy magnetic state. Second, we find a substantial change of the minimum energy interlayer distances with change of the magnetic state. On Cu(100) the most contracted minimum energy distance was found for the nonmagnetic solution with $\Delta z_{\text{N}} = 1.39\%$. For the ferromagnetic state a relaxation of $\Delta z_{\text{F}} = 4.02\%$ and for the antiferromagnetic state a relaxation of $\Delta z_{\text{AF}} = 5.41\%$ was determined. We find that the effect of the long range magnetic ground state on the relaxation is equally important as the formation of moments itself: the formation of a magnetic moment expands the interlayer distance by about 2.6% and the change in the magnetic state changes the interlayer distance by 1.4%. This coincides with the energy differences between the ferromagnetic state and the nonmagnetic state which is comparable to the energy difference between the antiferromagnetic state and the ferromagnetic one.

On Ag(001), the interlayer relaxations for the nonmagnetic, ferromagnetic, and antiferromagnetic Mn monolayers are determined to $\Delta z_{\text{N}} = -13.4\%$, $\Delta z_{\text{F}} = -6.75\%$, and $\Delta z_{\text{AF}} = -5.94\%$, respectively. The lattice constants of Ag is 14% larger than the lattice constant of Cu. Consequently the Mn atoms relax inwards on these substrates. Due to the large Mn moments, around $4 \mu_{\text{B}}$ on these substrates (recall the moment of Mn on Cu is slightly below $3 \mu_{\text{B}}$), the magneto-volume effect is very large. The ferromagnetic Mn monolayers experience a large expansion of their minimum energy interlayer distance of about 7%, much larger than for Cu and the magnetic configuration modifies this expansion by an other 1% to 2%. The impact of the magnetic order on the interlayer distance is within about 2%, but the magneto-volume effect due to the formation of large magnetic moments is much larger for Mn on Ag than for Mn on Cu. This is in line with the arguments based on energy differences. The energy difference between the antiferromagnetic state and the ferromagnetic state is for all Mn systems in the same ballpark of about 300 meV/Mn atom (cf. Table 1), while the formation energy of local moments is at large difference: about 200 meV for Mn on Cu but 1300 meV for Mn on Ag. This explains the large difference in the magneto-volume effects between Mn on Cu and Mn on Ag. In all cases the relaxations stabilize the ferromagnetic and antiferromagnetic phases, respectively.

Concluding, the atomic volume depends on the magnetism, mostly on the size of the moment and to a smaller extent on the magnetic state. An extreme example of this is the experimentally observed unusually large atomic buckling of the $c(2 \times 2)$ MnCu/Cu(001) [53] and $c(2 \times 2)$ MnNi/Ni(001) [53] surface alloys. In these alloys a buckling of the surface atoms of 0.30 Å (MnCu) [53] and 0.25 Å (MnNi) [53] was found. Although the atomic radii of Pd and Au are much larger than for Mn, the buckling of the $c(2 \times 2)$ CuPd/Cu(001) and $c(2 \times 2)$ CuAu/Cu(001) atoms was observed to just 0.02 Å [54] and 0.10 Å [55], respectively. It was shown that this

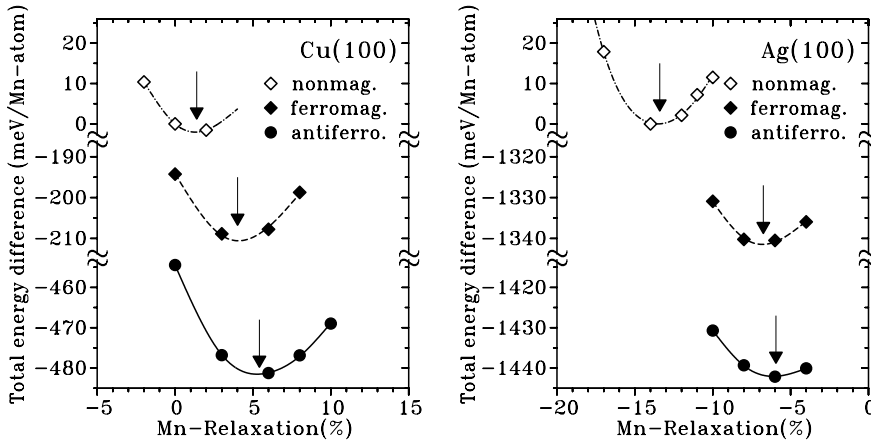


Fig. 15: Total energies as function of the interlayer relaxation for nonmagnetic (open diamonds), ferromagnetic (solid diamonds), and $c(2 \times 2)$ antiferromagnetic (solid circles) Mn monolayers on Cu(001) and Ag(001). The energy of the nonmagnetic monolayer at 0% relaxation was chosen as the origin of the total energy scale. The interlayer relaxation is given in relative units with respect to the interlayer distance of the substrate. The vertical arrows indicate the minimum energy interlayer relaxation.

buckling was a consequence of the magneto-volume effect, due to the large moments of Mn ($3.75 \mu_B$) in Cu [56] and Ni ($3.55 \mu_B$) [57].

4.2 (111) Oriented Monolayers on Nonmagnetic Substrates

4.2.1 Ferromagnetic Monolayers

The (0001) surface of an hcp crystal and the (111) surface of a fcc crystal establish a triangular lattice. Compared to the (100) surface the coordination number changes from 4 to 6, and the symmetry changes from fourfold to threefold or sixfold, respectively. Moreover, the differences in the magnetic properties between films on a square lattice and on a triangular lattice gives an estimate of the importance of the pseudomorphic growth condition for the magnetism of the films.

Figure 12 exhibits the general trend that the magnetic moments of the sixfold coordinated monolayers on Ag(111) are smaller in magnitude than those of the fourfold coordinated ones on Ag(001). On the Ag(111) surface we found magnetism for all $3d$ metals with the exception of Ti, which was very small anyway. There is nearly no difference between the monolayer moments of Mn, Fe, Co, and Ni on the differently oriented Ag substrates. A comparatively larger reduction of the magnetic moments is found at the beginning of the $3d$ series where the wavefunction is more extended than at the end of the series. Thus, changing the coordination number from 4 to 6, changes the local moments not significantly. One consequence of this result is that for monolayers which do not grow pseudomorphically on any substrate, but keep an average distance between monolayer atoms similar to the pseudomorphic films, no dramatic difference in the formation of large local moments are expected.

With the exception of Ru ($1.23 \mu_B$), and Rh ($0.67 \mu_B$) and a tiny moment for Ir ($0.05 \mu_B$) among

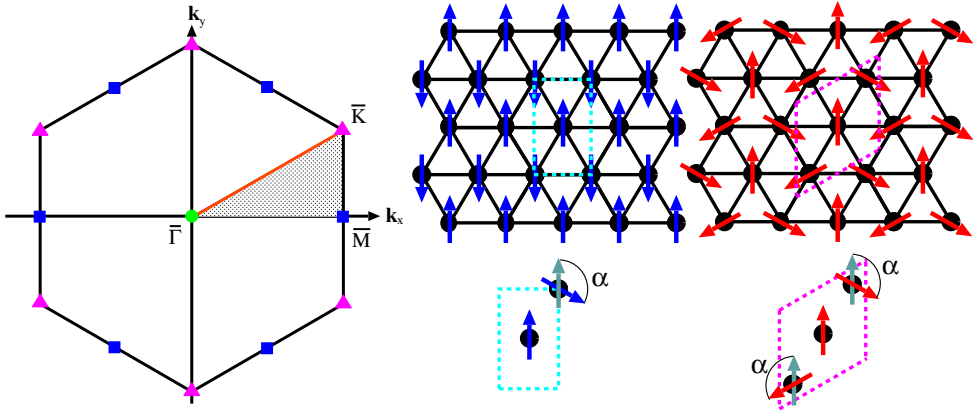


Fig. 16: (Left:) The hexagon shows the first BZ of the 2D hexagonal Bravais lattice. The gray-shaded area indicates the irreducible part. (Center:) The RW-AFM structure. (Right:) the coplanar non-collinear Néel (120°) structure. Indicated are the corresponding two- and three-atom unit cells and the continuous paths, which connect the corresponding magnetic structure to the FM state.

the $5d$ metals, no ferromagnetism was found for any other $4d$ and $5d$ monolayers on Ag(111). For the $4d$ metal monolayers Ru and Rh, the moments are reduced to about 70% of the (001) values and for the $5d$ metal Ir only a tiny magnetic moment of $0.05 \mu_B$, about 15% of the (001) value, remains. Obviously, the degree of the reduction of the magnetic moments due to the increase of the hybridization with the increase of the coordination number from 4 to 6, follows simply the increasing degree of delocalization of the d wavefunction when moving from the $3d$ to the $4d$ and $5d$ transition–metal wavefunctions.

4.2.2 Monolayers with Complex Spin Structures

Antiferromagnetic interactions on a triangular lattice are the origin of frustrated spin systems. In recent years the epitaxial growth of such ultra-thin films has been studied intensively by various experimental techniques. In particular, pseudo-hexagonal $c(8 \times 2)\text{Mn}$ films on Cu(100) [58], Mn films on the (111) surfaces of fcc Pd [59], Ir [60], Cu [61, 62, 63], and MgO [64] and on the (0001) surface of Ru [65] and Co [66] have been prepared and analyzed. But also other ultra-thin hexagonal films, e.g. Cr and V on Pt(111) and Ru(0001) [67, 68, 69], have been investigated.

To obtain an overview of all relevant spin-structures we develop first a zero-temperature phase diagram in the context of the Heisenberg model. As discussed in Sect. 2.2 the magnetic ground states are SSDWs, most likely with a commensurate propagation vector \vec{q}_\parallel located at the high-symmetry points in the first 2DBZ of a 2D Bravais lattice. For the 2DBZ of the triangular (hexagonal) lattice, displayed in Fig. 16 (Left), the high-symmetry points are the corner points $\bar{\Gamma}$, \bar{K} , and \bar{M} of the irreducible wedge of the 2DBZ (12DBZ). The $\bar{\Gamma}$ -point corresponds to the ferromagnetic solution. The \bar{K} -point corresponds to a 120° Néel state (Fig. 16 (Center)), a 2D coplanar spin structure with three atoms in a $(\sqrt{3} \times \sqrt{3}) R30^\circ$ unit cell for which the relative angle between the spins at the different sites is always 120° . The \bar{M} -point corresponds to row-wise antiferromagnetic (RW-AFM) configuration (Fig. 16 (Right)), which can be described by a

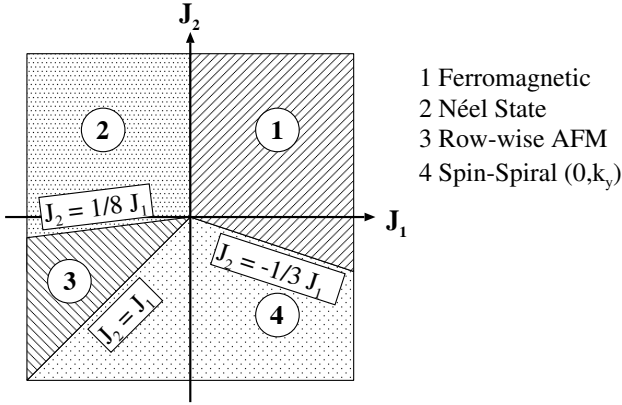


Fig. 17. Zero temperature phase-diagram in the (J_1, J_2) space for the triangular lattice indicating the regions of the four possible magnetic states.

rectangular unit cell with two antiferromagnetically aligned atoms. Magnetic ground states with incommensurate \vec{q}_{\parallel} -vectors are also possible preferentially with \vec{q}_{\parallel} -vectors from the connecting high-symmetry lines $\bar{M}-\bar{\Gamma}-\bar{K}-\bar{M}$.

Along the line $\bar{M}-\bar{\Gamma}-\bar{K}-\bar{M}$ we investigated the energetics within the Heisenberg model up to the second nearest-neighbor interaction, i.e. including the exchange constants J_1, J_2 . The results are summarized in Fig. 17 in terms of a zero-temperature phase diagram. Depending on the signs and values of J_1 , and J_2 four kinds of possible magnetic ground states exist: FM, RW-AFM, 120° Néel, and the SSDW. If J_2 is zero or positive (ferromagnetic) then there are only two possible magnetic ground states, determined by the sign of J_1 , the FM and the Néel state. But small values of J_2 are already sufficient to change the magnetic ground state and an infinite number of magnetic states becomes possible, the RW-AFM state or the incommensurate SSDW at any possible wave-vector \vec{q}_{\parallel} at the high-symmetry line $\bar{\Gamma}-\bar{M}$. Extending the model by including also J_3 , a magnetic state with a \vec{q}_{\parallel} at any high-symmetry line can become ground state.

Since the J 's are rapidly varying functions of the number of d electrons, ab-initio calculations are carried out to determine the element specific ground states. Since the calculations are very time consuming, the full overview has been worked out only for unsupported, free-standing monolayers (UML). Fig. 18 shows for the UMLs with the Cu lattice constant the total energy $E(\vec{Q}_{\parallel})$ and the magnetic moments $M(\vec{Q}_{\parallel})$ calculated for a discrete set of the spin-spiral \vec{Q}_{\parallel} vectors along the high-symmetry lines. Among all the SSDWs calculated, the high-symmetry points have the lowest energies: the 120° Néel state (\bar{K} -point) for Cr(111), the RW-AFM state (\bar{M} -point) for Mn(111), and the FM state ($\bar{\Gamma}$ -point) for Fe(111). For Fe and Mn, the $M(\vec{Q}_{\parallel})$ are nearly a constant, but the Cr moments change drastically, as no ferromagnetic solution could be found for Cr(111). One more interesting observation is the local minimum of $E(\vec{Q}_{\parallel})$ for Mn on the line $\bar{\Gamma}-\bar{K}$, which is only 21 meV higher in energy than the RW-AFM state. We expect that a small change in the d -band filling, e.g. due to alloying with Fe, may change the energetics and an incommensurate SSDW may become the magnetic ground state.

For Mn, the lowest energy magnetic state found so far is the RW-AFM state, which corresponds to the commensurate SSDW state with one single \vec{Q}_{\parallel} -vector at the \bar{M} -point of the 2DBZ, and the RW-AFM is also called single- \vec{Q}_{\parallel} (1Q) state. In the 2DBZ there are three \bar{M} -points corresponding to the three possible directions of the long axis of the RW-AFM unit cell on a triangular

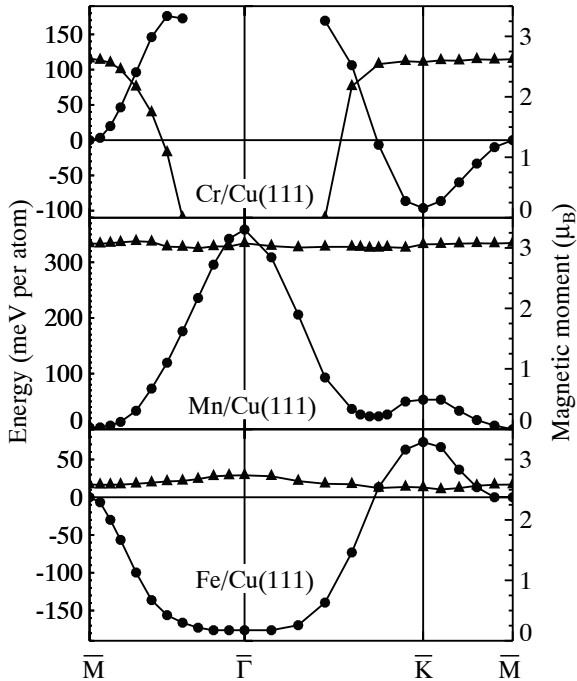


Fig. 18. Calculated total energies (circles, left scale) and magnetic moments (triangles, right scale) for spin-spiral states in 3d-UMLs with the Cu(111) geometry as function of the 2D wave vector \vec{Q}_{\parallel} along the high symmetry lines of the 2DBZ. The energy is shown relative to the energy of the RW-AFM state.

lattice. They are equivalent in symmetry but are different to each other with \vec{Q}_{\parallel} -vectors, $\vec{Q}_{\parallel}^{(k)}$, for $k = 1, 2, 3$. Within the Heisenberg model, the energy of each SSDW, denoted by one of the three wave vectors $\vec{Q}_{\parallel}^{(k)}$ or any SSDW being an orthogonalized linear combination of those, are degenerate. Higher order spin interactions (4) and (4) may lift this degeneracy and a so-called triple- \vec{Q}_{\parallel} (3Q)-state, may become lower in energy. The 3Q-state is a three-dimensional non-collinear spin-structure on a 2D lattice (see Fig. 19) with four chemically identical atoms per surface unit-cell, where the relative angle between all nearest-neighbor spins is given by the tetrahedron angle of 109.47° . The 3Q-state is formed as a linear combination of the three RW-AFM (1Q) structures orthogonal in spin-space, each having one of the three $\vec{Q}_{\parallel}^{(k)}$ -vectors of the \bar{M} -points:

$$\vec{m}(\vec{r} + \vec{R}_i) = m(\vec{r}) \times \frac{1}{\sqrt{3}} \sum_{k=1}^3 e^{i\vec{Q}_{\parallel}^{(k)} \cdot \vec{R}_i} \hat{e}^{(k)}, \quad (22)$$

where the $\hat{e}^{(k)}$ are orthogonal unit vectors in spin space. We see that in the nearest-neighbor approximation to the higher order exchange contributions the sign of K_1 and B_1 determine the sign of the energy difference $\Delta E = E_{3Q} - E_{1Q} = 16/3S^4(2K_1 + B_1)$ and thus whether the 3Q or the 1Q state becomes the magnetic ground state. From the ab-initio calculations for the Mn UML in the geometry of Cu(111) we [3] found that the 3Q-state is 15 meV/atom lower in energy than the 1Q-state.

Calculations including the Cu(111) substrate show that the energy differences between different magnetic states change due to the presence of the substrate, but the magnetic ground state remains unaltered: Cr/Cu(111) exhibits the 120° Néel state ($2.35 \mu_B$), Mn/Cu(111) the 3Q-structure ($2.74 \mu_B$), which is 17 meV lower in energy than the 1Q-state ($3.00 \mu_B$), and

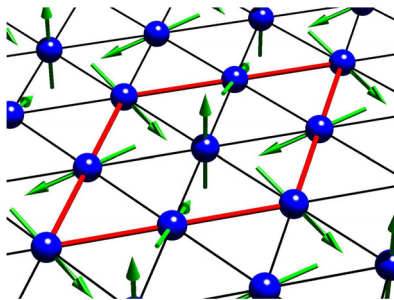


Fig. 19. An image of the magnetic 3Q-structure, with spins pointing in all three directions of the spin-space. Note that, due to the neglect of the spin-orbit interaction only the relative orientation of the moments is specified.

Fe/Cu(111) is ferromagnetic ($2.63 \mu_B$). On the Ag(111) substrate [70] the overall picture is the same, but two differences were noticed: V/Ag(111) is magnetic ($2.19 \mu_B$) and exhibits as Cr/Ag(111) ($3.65 \mu_B$) the 120° Néel state and the magnetic ground state of Mn/Ag(111) is the RW-AFM state ($3.91 \mu_B$) and not the 3Q-state ($3.88 \mu_B$). Fe/Ag(111) is ferromagnetic ($3.02 \mu_B$). We believe that the complex spin-structures presented here, can be resolved using the spin-polarized scanning tunneling microscope in the constant-current mode [71, 70].

4.3 Magnetic Substrate: Magnetic Exchange Coupling of 3d Metals on Fe(001)

4.3.1 Monolayers

3d-metal monolayers on Fe(001) are prototypical systems where the in-plane magnetic interactions, described by the exchange coupling parameter J_{\parallel} , compete with the strong magnetic interactions J_{\perp} between the monolayer and the substrate. Depending on the signs and values of J_{\parallel} and J_{\perp} , complex spin structures as ground states can be anticipated. Finally, total-energy calculations are required to determine the minimum-energy magnetic-state among the various metastable solutions. We recently carried out calculations [72, 73] which considered three competing spin structures: the $p(1 \times 1)$ ferromagnetic (FM), the $p(1 \times 1)$ layered antiferromagnetic (LAF), and the $c(2 \times 2)$ ferrimagnetic (FI) spin configurations shown in Fig. 20. Figure 21 summarizes the results from calculations for structurally unrelaxed monolayers, i.e. where the monolayer atoms are located at the ideal, bulk truncated, pseudomorphic Fe atom sites. For most 3d metal overlayers (Cr, Mn, Fe, Co) on Fe(001) all three configurations exist and are

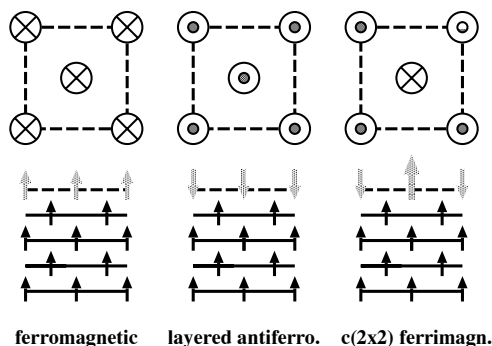


Fig. 20. Schematic representation of a ferromagnetic, a layered antiferromagnetic, and a $c(2 \times 2)$ (anti)ferrimagnetic superstructure of a monolayer film (broken line) grown as overlayer on a magnetic substrate (full line). Upper panel shows view onto the surface, lower panel shows side-view. Arrows indicate the relative spin direction at the positions of the atoms.

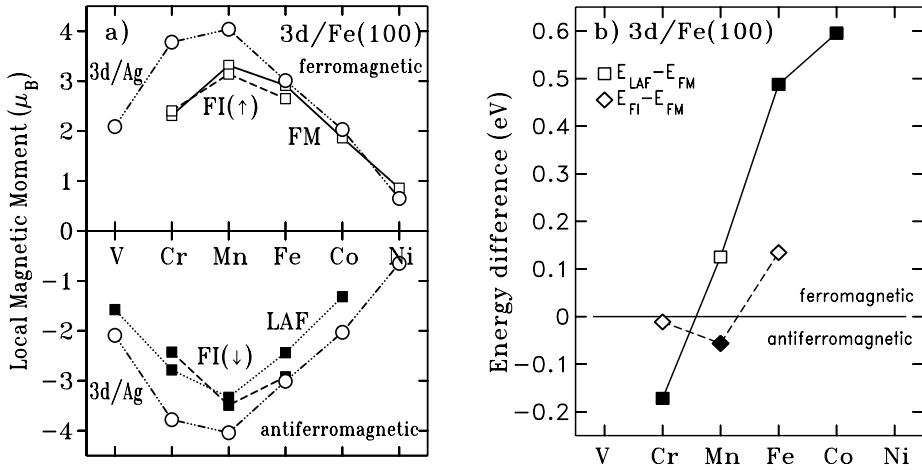


Fig. 21: **a)** Left Figure: Local magnetic moments of unrelaxed 3d transition-metal monolayers on Fe(001). Positive (negative) sign of moments indicates an (anti)ferromagnetic, FM (AF), spin alignment to the Fe substrate, emphasized by open (filled) symbols. Shown are results of three different spin configurations: $p(1 \times 1)$ FM (solid line), $p(1 \times 1)$ LAF (dotted line), and the $c(2 \times 2)$ FI (dashed lines) for positive and negative moments. Figure is complimented with results for 3d monolayers on Ag(001) (\circ connected by dash-3-dotted line). As the Ag substrate is nonmagnetic, ferro- and antiferromagnetic spin alignment is indistinguishable and moments are identical and are shown twice, once for positive and negative sign. **b)** Right Figure: Total energy difference $\Delta E_1 = E_{LAF} - E_{FM}$ between the $p(1 \times 1)$ layered antiferromagnetic and the ferromagnetic coupling (squares connected by solid lines) and $\Delta E_2 = E_{FI} - E_{FM}$ between the $c(2 \times 2)$ ferrimagnetic and the $p(1 \times 1)$ ferromagnetic coupling (diamonds connect by dashed lines) of 3d transition-metal monolayers with Fe(001). The ferromagnetic (layered antiferromagnetic or ferrimagnetic) coupling has lower energy for $\Delta E > 0$ (< 0), and is therefore favored. The layered antiferromagnetic coupling is preferred over the ferrimagnetic one if $\Delta E_1 < \Delta E_2$. Filled square or diamond indicate the magnetic ground state. For V and Ni only one magnetic state has been found.

energetically stable. Only the V and Ni monolayers were found to couple exclusively layered antiferromagnetically or ferromagnetically, respectively, to the Fe(001) substrate. Surprisingly, the ferromagnetic ($M > 0$), the layered antiferromagnetic ($M < 0$) and the two different magnetic moments ($M_1 > 0$ and $M_2 < 0$) for the ferrimagnetic phase are all similar in size. The largest magnetic moment of about $3 \mu_B$ was found for Mn, and then the magnetic moments drop for elements left and right of Mn, reminiscent of the behavior on the noble-metal substrates.

In order to see the effect of the hybridization between the substrate and the overlayer on the size of the local moments, the local magnetic moments of 3d-metal monolayers on Ag(001) [39] are included for comparison. Fe ($a_{\parallel} = 5.33$ a.u.) and Ag ($a_{\parallel} = 5.51$ a.u.) have very similar in-plane lattice constants and thus very similar in-plane $d-d$ hybridizations may be expected for the monolayer, but the $d-d$ hybridization across the interface is largely different. From Fig. 21a one infers that the magnetic moments for the Fe, Co, and Ni monolayers are rather independent on the substrate, but increasing deviations are obtained for the monolayer moments in the sequence from Mn to V. The extent of the 3d wave function increases for chemical elements from the end

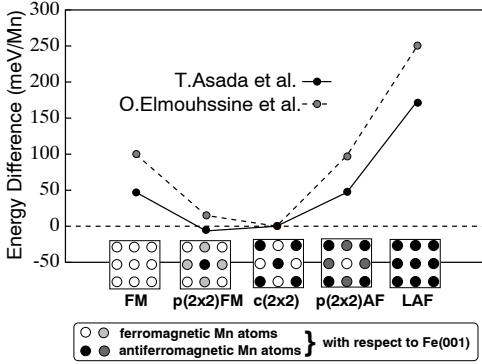


Fig. 22. Relative energy $E - E_{c(2 \times 2)}$ for the five magnetic configurations. The small energy difference between the $c(2 \times 2)$ FI state and the $p(2 \times 2)$ FM configuration indicates that the two solutions are nearly degenerate ground states.

of the $3d$ series to the beginning of the series. Accordingly, the d - d hybridization within the monolayer and between the monolayer and the Fe substrate increases. As a consequence, the magnetic moments for Mn, Cr, and V overlayers are visibly reduced.

Since the local magnetic moments of the three different magnetic states for Cr, Mn, Fe, and Co monolayers on Fe(001) are very similar in size, total-energy calculations have been performed to determine the minimum energy magnetic configuration. The energy difference $\Delta E_1 = E_{\text{LAF}} - E_{\text{FM}}$ between the layered antiferromagnetic and ferromagnetic configuration and $\Delta E_2 = E_{\text{FI}} - E_{\text{FM}}$ between the $c(2 \times 2)$ ferrimagnetic and the ferromagnetic configuration, ignoring again any monolayer relaxation, are shown in Fig. 21b. For V and Ni monolayers, which show only one magnetic solution, no data points are included. As has been reported in the literature [74, 72, 75] we find with the exception of Cr, that the ferromagnetic coupling ($\Delta E_1 > 0$) is energetically always more favorable than the layered antiferromagnetic one and that for Cr and Mn the ferrimagnetic coupling ($E_2 < 0$) is energetically preferred over the ferromagnetic one. For Fe, Co, and Ni, the ferromagnetic solution is the most stable one. When we compare for Cr or Mn the energies among the three different magnetic phases, we find that for Cr the layered antiferromagnetic coupling is the magnetic ground state, energetically followed by the ferrimagnetic and the ferromagnetic coupling, which are metastable phases. The calculated total-energy differences between FM and LAF configurations and between FM and FI show some differences to those of Handschuh *et al.* [72] mostly due to the different choice of the in-plane lattice constant. Summarizing, (i) the magnetic ground state structures are LAF for V and Cr, FI for Mn, FM for Fe, Co, and Ni. (ii) For the Mn monolayer we find a second spin configuration with an energy of about 55 meV/Mn above the ground-state structure. Therefore, extending the search for the magnetic ground state of Mn to larger surface unit-cells may lead to a more complicated ground-state spin-structure. Elmouhssine *et al.* [76] and Asada *et al.* investigated the possibility of additional low-energy spin-structures in the $p(2 \times 2)$ surface unit-cell containing four Mn surface atoms. Two additional spin-structures were included: the $p(2 \times 2)$ FM magnetic structure with three Mn atoms out of four coupling ferromagnetically to the Fe substrate and one Mn atom coupling antiferromagnetically, as well as the $p(2 \times 2)$ AF structure, which is the layered antiferromagnetic version of $p(2 \times 2)$ FM, where three Mn atoms couple antiferromagnetically and one atom couples ferromagnetically to Fe. Indeed the calculations reveal that on Fe(001), the Mn $c(2 \times 2)$ FI, and the $p(2 \times 2)$ FM are nearly degenerate ground states. This is obvious from Fig. 22, which displays the energies of the different configurations relative to the $c(2 \times 2)$ FI state energy. Tight-binding linear muffin-tin orbital calculations by Elmouhssine *et al.* found that the $p(2 \times 2)$ FM superstructure is 15 meV higher in energy than

the $c(2 \times 2)$ one, while Asada *et al.* found by FLAPW calculations that the total energy of the $p(2 \times 2)$ FM superstructure is slightly lower (~ 6.4 meV/Mn) than the $c(2 \times 2)$ FI structure. Not shown here but the interlayer distances of relevant magnetic configurations had been fully optimized by the use of force calculations, and these relaxations do not change this picture. The energy differences are comparable to the thermal energy at room temperature. Thus surface roughness and thermal excitations in true experimental situations could lead to the coexistence of these two magnetic configurations and thus the appearance of magnetic domains within the Mn monolayer. At present one cannot exclude the possibility of magnetic states with even lower energy not investigated yet.

4.3.2 Doublelayers

In order to demonstrate the complexity of the systems we show here also the results of the $3d$ metal bilayers on Fe(001). For the doublelayer systems we have examined all possible magnetic configurations within the $c(2 \times 2)$ unit cell. With the exception of Mn all stable magnetic configurations found have the magnetic $p(1 \times 1)$ structure. The magnetic ground states are the $p(1 \times 1)$ LAF one for V, Cr, and Mn, and the $p(1 \times 1)$ FM one for Fe, Co, and Ni bilayers on Fe(001). For Mn we found in addition to the $p(1 \times 1)$ LAF ground-state structure also the superstructure ($[\uparrow\downarrow]_S \downarrow_{S-1} \mid \uparrow \text{Fe}$) as stable solution with a total energy of 43.2 meV/Mn higher than the LAF structure. The magnetic moments for the bilayer systems are collected in Fig. 23. Please note for the case of the LAF Mn doublelayer the almost vanishing magnetic moment of the subsurface atom. Furthermore, for the Mn bilayer, in addition to those two configurations, the ground state ($\uparrow_S \downarrow_{S-1} \mid \uparrow \text{Fe}$) and the superstructure stated just above, we also found a third configuration, ($\downarrow_S \uparrow_{S-1} \mid \uparrow \text{Fe}$), which is about 9 meV/Mn higher in energy than the ground state. Thus there exist three states within an energy range corresponding to about 400 K. We believe that this gives already a glimpse of the difficulties involved in dealing with thicker Mn overlayers on Fe(001) [77].

For a Cr monolayer the measured magnetic moment was found to be at most $1 \mu_B$ [78, 79], which is less than half of the theoretical prediction [74, 72]. It was also reported that the layer-by-layer growth leads to a strong intermixing with the substrate Fe layers [80, 81, 82]. Mn overlayers seem to be even much more involved. There is a general experimental consensus that for Mn around one ML coverage the signals related to the magnetization disappear. The microscopic origin for this observation is under strong debates. One explanation supported by

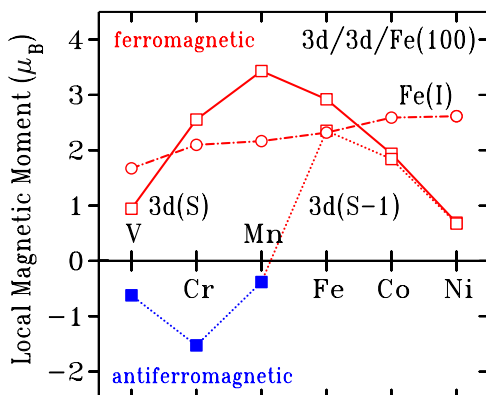


Fig. 23. Local magnetic moments (M) for the ground-state spin configurations of unrelaxed $3d$ transition-metal doublelayers on Fe(001). The solid line denotes the $3d$ surface atoms ($3d(S)$) aligned parallel ($M > 0$) to the Fe substrate, the dotted line denotes the $3d$ subsurface atoms ($3d(S-1)$), whose coupling changes from LAF ($M < 0$) to FM ($M > 0$) from early to late $3d$ elements. The chained line denotes the interface Fe atoms ($Fe(I)$).

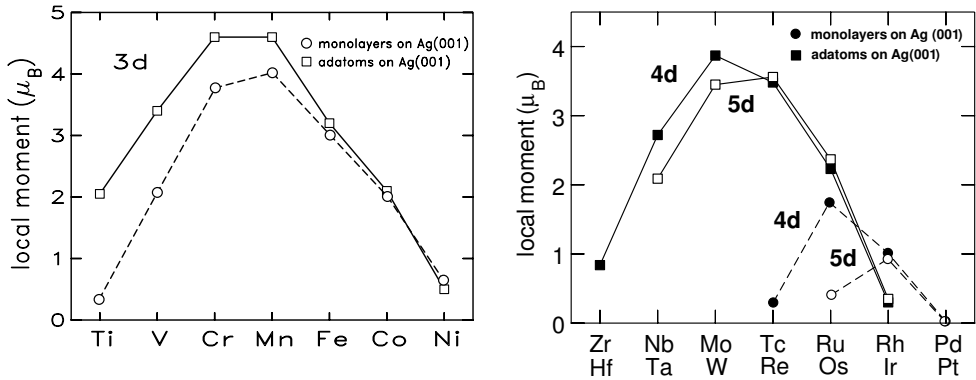


Fig. 24: Local magnetic moments calculated for 3d [85] (left), 4d (right, solid symbols), and 5d (right, empty symbols) transition–metal adatoms at the hollow–site of Ag(100) (squares connected by full lines) [84] and monolayers as overlayers on Ag(100) [46] (circles connected by dashed lines).

theory [72, 75] is a possible onset of the in-plane ferrimagnetic coupling. On the other hand, strong interfacial alloying has been observed [83], which may lead to the same results. A third option is the possibility of a doublelayer growth mode, which may also lead to the disappearance of magnetic signals. The difficulty in controlling and characterizing the morphology of the interface seems to be intimately related to the difficulties in understanding of the interfacial magnetism of those systems. A complete picture requires additional theoretical investigations including the the possibility of interdiffusion and surface alloying.

5 Atomic-Scale Structures

5.1 Adatoms

Single transition-metal adatoms adsorbed on (100) substrates of Cu, Ag, Au [84, 85], Pd and Pt [86] have been investigated by first-principles calculations. When the 3d overlayer and adatom moments on Ag(100) are compared as shown in Fig. 24, a surprising similarity in the general trend and the magnitude of the magnetic moments is found. Obviously the local moments of monolayers follow Hund’s first rule of the adatoms. In other words, if we decompose the DOS according to (13) in terms of the local (χ_{00}) and the interatomic non-local susceptibilities (χ_{0i} , $i > 1$), then for the adatoms the non-local susceptibilities are basically zero, by definition, but also for the monolayers χ_{00} dominates over χ_{0i} . For Fe, Co, and Ni, monolayer and adatom, the magnetic moments are about equal and fully saturated. This will not change for other atomic-scale structures such as chains. For example recent calculations of one-atomic Fe, Co, Ni wires along the $\langle 111 \rangle$ -type step-edge of the Pt(111) surface exhibit local moments of 3.18 μ_B , 2.12 μ_B , 0.83 μ_B , respectively. From Mn to Ti, monolayer and adatom moments deviate systematically due to the increasing extent of 3d wavefunction and the respective increase of the d – d hybridization in the monolayer.

For the 4d and 5d transition-metal adatoms the comparison to the monolayers on Ag(100) looks radically different. While the adatoms still follow Hund’s first rule with maximal moments at

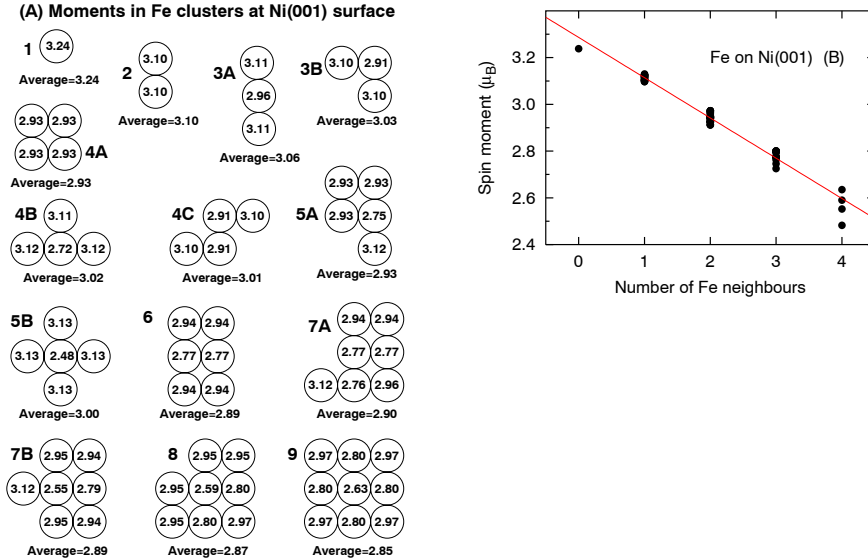


Fig. 25: A: Spin moment (in μ_B) of atoms of Fe clusters at Ni(001) surface, and average (per atom) moment of the clusters (the view is surface-adapted, i.e., rotated by 45° with respect to the in-plane fcc cubic axes; the clusters are viewed from the top, i.e., all atoms lie on the surface). B: Linear trend for the atomic Fe spin moment as function of the coordination to Fe neighbors [19].

the center of each series, the magnetism of monolayers is obviously largely determined by the non-local susceptibilities χ_{0i} which add an essential contribution to χ_{00} necessary to fulfill the Stoner criterion (9). This is a consequence of the large extent of the $4d$ and $5d$ wavefunctions. Since χ_{0i} depends on all details of the local environment, each atomic-scale structure of $4d$ and $5d$ metals will have a different collection of magnetic moments. This observation motivated the work on atomic-scale clusters.

5.2 Clusters

Small atomic clusters on surfaces constitute very interesting subjects, as their electronic structure and subsequently the magnetic properties depend in addition to other factors mentioned above, on the individual cluster shape and size. In order to explore the consequences of this statement we explore the spin-moment of Fe on a Ni(100) surface [19]. The clusters considered are shown schematically in Fig. 25, viewed from the top (all atoms lie on the surface). The view is adapted to the surface geometry, meaning that it is rotated by 45° with respect to the in-plane fcc cubic axes of the underlying substrate lattice. The smallest cluster is a single Fe adatom, while the largest consists of 9 Fe atoms. On each atom, the calculated spin moment is written, and the average (per atom) moment of each cluster is also given. The Fe moment is always ferromagnetically coupled to the Ni substrate moment. Already at a first glance it is obvious that the average moment of the clusters depends on the cluster size. The single adatom has manifestly the highest moment ($3.24\mu_B$), while the 9-atom cluster shows a lower average moment of $2.85\mu_B$.

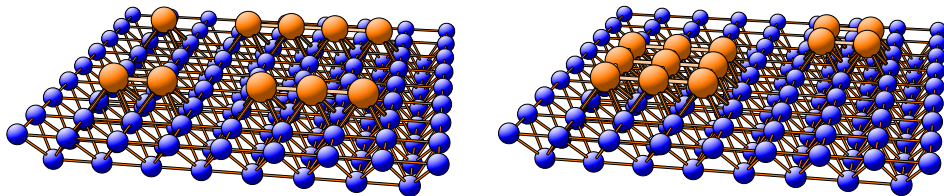


Fig. 26: *Magnetic clusters of a particular transition metal deposited on an (100) oriented Ag substrate.*

From what has been said in Section 2.4 this behavior is expected on the grounds of hybridization of the atomic d levels with the neighbors. Atoms in larger clusters have, on the average, higher coordination, thus their d wavefunctions are more hybridized; this leads to lesser localization and lesser tendency to magnetism.

To pursue this idea further, we tried to correlate the local atomic spin moment to the coordination of each atom, irrespective of the form or size of the cluster. For instance, let us focus on all Fe atoms which have only one first Fe neighbor, i.e., $N_c = 1$ (the coordination to the substrate is the same, $N_s = 4$, for all Fe atoms). Such atoms appear in the clusters with size 2, 3, 4, 5, and 7; there are, in total, 10 such examples (having excluded cases which are trivially equivalent by symmetry). All of them have spin moments ranging in the small interval between 3.10 and $3.13\mu_B$. Similarly, for the Fe atoms with two Fe neighbors the spin moment ranges from 2.91 to $2.97\mu_B$. Collecting all possible cases, from $N_c = 0$ (single adatom) to $N_c = 4$, we present the results in Fig. 25B. One finds an almost linear dependence of the spin moment on the coordination number. In agreement with the analysis of the $3d$ transition-metal films Fe has a strong intra-atomic exchange field, arising from rather localized $3d$ wavefunctions resulting in strong intra-atomic susceptibility.

In many cases for homo-atomic and mass-selected ferromagnetic clusters, it is very difficult to address experimentally the magnetic properties of each individual cluster or even each atom in a cluster. Often just the average magnetic moment of clusters of particular size or the average local magnetic moment per atom averaged over an ensemble of clusters of the same size but different shapes can be determined. Using this scaling behavior it is possible to estimate the magnetic moments of clusters if the shape is known.

In the light of what has been said above for the $4d$ and $5d$ adatoms on surface this is not the general case for arbitrary atoms. For example, the magnetism of small $4d$ and $5d$ clusters on Ag(100) show highly non-local susceptibilities, resulting even in an increase of the spin moment with coordination. This is connected to the larger extent of the $4d$ states compared to the $3d$ of Fe. The magnetic properties of several linear chains (C) and plane islands (I) of $4d$ and $5d$ adatoms have been calculated [87] and are shown in Fig. 26. In particular, linear chains of 2 (dimers, C2), 3, and 4 adatoms (C3 and C4) have been considered, being oriented in the (110) direction as well as three compact islands with 4, 5, and 9 adatoms (I4, I5, and I9).

Figure 27 shows the calculated moments per adatom for these nanostructures. Since several nonequivalent atoms exist for the clusters C3, C4, I5, and I9, only the average moment is given. For the linear chains quite large moments are obtained, but the behavior with size is non-regular. While the C2 and C4 moments are very similar, the C3 moments of Mo and Tc are much smaller. In this context it is interesting to compare the moments of the inner and outer chain atoms. For Mo and Tc the outer atoms of C3 and C4 have larger moments than the inner ones. In the C4 chain, for instance, the two inner Mo atoms have moments of $1.85\mu_B$, while the outer atoms

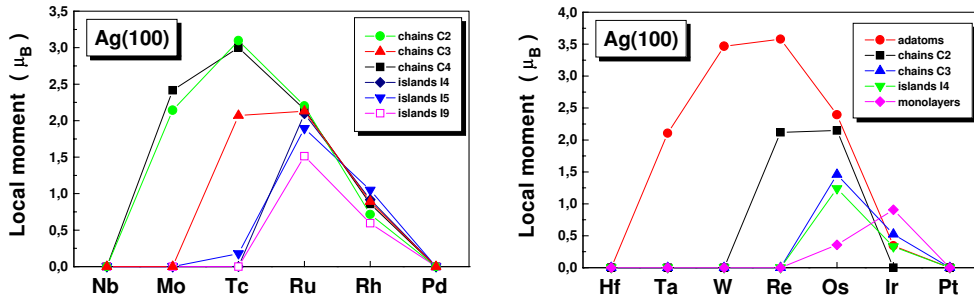


Fig. 27: Average magnetic moment per adatom for 4d (left) and 5d (right) clusters [87].

carry 3.00 μ_B . Moving to Ru and Rh the situation changes. In the Ru chains both types of atoms have about the same moments, whereas in the case of Rh the inner atoms carry larger moments. In the Rh C4 chain the inner atoms have moments of 0.96 μ_B but the outer ones only 0.76 μ_B . This is because the higher coordination of the inner atoms tends to enhance the moments for Rh while Ru is an intermediate case being insensitive to environmental changes. The large moments obtained for all three chain structures indicate that infinite chains of these atoms should also show appreciable moments.

For the linear structure considered we also obtain antiferromagnetic solutions being the most stable configurations in the middle of the series. The moments can be quite large. For instance, for the Mo chains C2, C3, and C4 the atomic moments are larger than 3 μ_B .

For the compact islands (I4, I5, and I9) the hybridization effects within the cluster are even larger. Similar to magnetic monolayers [88, 45, 89] we find only appreciable moments for the Ru and Rh nanostructures, but no or very small moments for Mo and Tc. This is a consequence of the large spatial extent of 4d wave functions being more important for the compact islands than for the chain structures. Within the Ru structures I5 and I9 we observe that the outer atoms carry a larger moment than the inner ones, the same effect as found above for the linear structure of Mo and Tc. For Rh the situation is more complicated. For the I5 island the inner moment (1.00 μ_B) is larger than the outer one (0.66 μ_B), in agreement with the above rule, while the central atom in the I9 cluster has a very small moment of 0.16 μ_B , and the outer atoms have moments of 0.62 μ_B and 0.64 μ_B . Thus by comparing the islands with the chain structures, not only the peak of the moment curve is shifted to even larger valences, i.e., from Tc to Ru, but also the transition from surface enhancement of the moments to surface suppression is shifted: For the chains this turnover occurs at Ru, but for the more compact islands at about Rh. The very small moment obtained for the central atom of I9 seems to be in conflict with the results of monolayers for a Rh overlayer on Ag (100) which should have a moment of about 1 μ_B . Calculations for larger Rh islands lead for the inner Rh atoms to considerably larger moments (0.66 μ_B). Thus we conclude from these calculations, as well as from the strong difference obtained for the different linear chains C2, C3, and C4, that the moments of the 4d clusters show an unusual and oscillatory dependence on the cluster size.

References

- [1] M. Donath, Surf. Sci. Rep. **20**, 251 (1994).
- [2] S. Blügel, Appl. Phys. A **63**, 595 (1996).
- [3] P. Kurz, G. Bihlmayer, K. Hirai, and S. Blügel, Phys. Rev. Lett **86**, 1106 (2001).
- [4] P. Hohenberg and W. Kohn, Phys. Rev. **136**, B864 (1964).
- [5] U. von Barth and L. Hedin, J. Phys. C. **5**, 1629 (1972).
- [6] J. Kübler, *Derivation of the single-particle schrödinger equation: Density and spin-density functional theory and the magnetic susceptibility, noncollinear ground states, towards the curie temperature* (1995), lecture Notes from: Workshop on Condensed Matter Physics.
- [7] J. Perdew, J. Chevary, S. Vosko, K. Jackson, M. Pederson, D. Singh, and C. Fiolhais, Phys. Rev. B **46**, 6671 (1992).
- [8] V. L. Moruzzi, J. F. Janak, and A. R. Williams, *Calculated Electronic Properties of Metals* (Pergamon, New York, 1978).
- [9] M. Pajda, J. Kudrnovsky, I. Turek, V. Drchal, and P. Bruno, Phys. Rev. B **64**, 174402 (2001).
- [10] L. M. Sandratskii, Adv. in Phys. **47**, 91 (1998).
- [11] M. Takahashi, J. Phys. C **10**, 1289 (1977).
- [12] K. Terakura, N. Hamada, T. Oguchi, and T. Asada, J. Phys. F: Met. Phys. **12**, 1661 (1982).
- [13] T. Asada and S. Blügel, Phys. Rev. Lett **79**, 507 (1997).
- [14] S. V. Tyablikov, *Methods of Quantum Theory of Magnetism* (Plenum Press, New York, 1967).
- [15] R. P. Erickson and D. L. Mills, Phys. Rev. B **43**, 11527 (1991).
- [16] J. A. C. Bland and B. Heinrich, eds., *Thermodynamic Properties of Ultrathin Ferromagnetic Films* (Springer-Verlag, Berlin/Heidelberg, 1994), chap. D. L. Mills, p. 91.
- [17] O. Gunnarsson, J. Phys. F: Met. Phys. **6**, 587 (1976).
- [18] J. F. Janak, Phys. Rev. B **16**, 255 (1977).
- [19] P. Mavropoulos, S. Lounis, R. Zeller, and S. Blügel, submitted to Appl. Phys. A. (2005).
- [20] C. Rau, C. Liu, A. Schmalzbauer, and G. Xing, Phys. Rev. Lett. **57**, 2311 (1986).
- [21] S. C. Wu, K. Garrison, A. Begley, F. Jona, and P. Johnson, Phys. Rev. B **49**, 14081 (1994).
- [22] A. Goldoni, A. Baraldi, G. Comelli, S. Lizzit, and G. Paolucci, Phys. Rev. Lett. **82**, 3156 (1999).

- [23] T. Bryk, D. M. Bylander, and L. Kleinman, Phys. Rev. B **61**, R3780 (2000).
- [24] R. Robles, J. Izquierdo, A. Vega, and L. C. Balbás, Phys. Rev. B **63**, 172406 (2001).
- [25] I. G. Batyrev, J.-H. Cho, and L. Kleinman, Phys. Rev. B **63**, 172420 (2001).
- [26] I. Morrison, D. M. Bylander, and L. Kleinman, Phys. Rev. Lett. **71**, 1083 (1993).
- [27] J.-H. Cho and M. Scheffler, Phys. Rev. Lett. **78**, 1299 (1997).
- [28] S. Ohnishi, C. L. Fu, and A. J. Freeman, J. Magn. Magn. Mater. **50**, 161 (1985).
- [29] R. L. Fink, C. A. Ballentine, J. L. Erskine, and J. A. Araya-Pochet, Phys. Rev. B **41**, 10175 (1990).
- [30] G. Bihlmayer, T. Asada, and S. Blügel, Phys. Rev. B **62**, R11937 (2000).
- [31] M. Weinert, S. Blügel, and P. D. Johnson, Phys. Rev. Lett. **71**, 4097 (1993).
- [32] I. Turek, S. Blügel, and J. Kudrnovský, Phys. Rev. B **57**, R11065 (1998).
- [33] S. Handschuh, XXX, Ph.D. thesis, University of Cologne (199?).
- [34] W. M. Lomer, Proc. Phys. Soc. London **80**, 825 (1962).
- [35] A. M. N. Niklasson, B. Johanson, and L. Nordstöm, Phys. Rev. Lett. **82**, 4544 (1999).
- [36] A. M. N. Niklasson, J. M. Wills, and L. Nordstöm, Phys. Rev. B **63**, 104417 (2001).
- [37] J. A. Stroschio, D. T. Pierce, A. Davies, R. J. Celotta, and M. Weinert, Phys. Rev. Lett. **75**, 2960 (1995).
- [38] M. Kleiber, M. Bode, R. Ravlic, and R. Wiesendanger, Phys. Rev. Lett. **85**, 4606 (2000).
- [39] S. Blügel and P. H. Dederichs, Europhys. Lett. **9**, 597 (1989).
- [40] S. Blügel, Europhys. Lett. **7**, 743 (1988).
- [41] X. Nie, S. Heinze, G. Bihlmayer, and S. Blügel, *Ferromagnetism and Antiferromagnetism of 3d Transition Metal Monolayers on W(110)* (2001).
- [42] T. Asada and S. Blügel, Physica B **237-238**, 359 (1997).
- [43] S. Blügel, D. Drittler, R. Zeller, and P. H. Dederichs, Appl. Phys. A **49**, 547 (1989).
- [44] J. Redinger, S. Blügel, and R. Podloucky, Phys. Rev. B **51**, 13582 (1995).
- [45] S. Blügel, Europhys. Lett. **18**, 257 (1992).
- [46] S. Blügel, Phys. Rev. Lett. **68**, 851 (1992).
- [47] B. Újfalussy, L. Szunyogh, and P. Weinberger, Phys. Rev. B **51**, 12836 (1995).
- [48] A. J. Freeman and C. L. Fu, J. Appl. Phys. **61**, 3356 (1987).

- [49] M. Stampanoni, A. Vaterlaus, D. Pescia, M. Aeschlimann, F. Meier, W. Dürr, and S. Blügel, *Phys. Rev. B* **37**, 10380 (1988).
- [50] J. E. Ortega and F. J. Himpsel, *Phys. Rev. B* **47**, 16441 (1993).
- [51] S. Heinze, M. Bode, A. Kubetzka, O. Pietzsch, X. Nie, S. Blügel, and R. Wiesendanger, *Science* **288**, 1805 (2000).
- [52] M. Bode, S. Heinze, M. Hennefarth, O. Pietzsch, A. Kubetzka, M. Getzlaff, R. Wiesendanger, X. Nie, G. Bihlmayer, and S. Blügel, *Phys. Rev. B* **66**, 237205 (2002).
- [53] M. Wuttig, C. C. Knight, T. Flores, and Y. Gauthier, *Surf. Sci.* **292**, 189 (1993).
- [54] S. C. Wu, S. H. Lu, Z. Q. Wang, C. K. C. Lok, J. Quinn, Y. S. Li, D. Tian, and F. Jona, *Phys. Rev. B* **38**, 5363 (1988).
- [55] Z. Q. Wang, Y. S. Li, C. K. C. Lok, J. Quinn, and F. Jona, *Solid State Commun.* **62**, 181 (1987).
- [56] M. Wuttig, Y. Gauthier, and S. Blügel, *Phys. Rev. Lett.* **70**, 3619 (1993).
- [57] O. Rader, W. Gudat, C. Carbone, E. Vescovo, R. Kläsches, S. Blügel, R. Kläsches, W. Eberhardt, M. Wuttig, J. Redinger, and F. J. Himpsel, *Phys. Rev. B* **55**, 5404 (1997).
- [58] T. Flores, M. Hansen, and M. Wuttig, *Surf. Sci.* **279**, 251 (1992).
- [59] D. Tian, H. Li, S. Wu, F. Jona, and P. Marcus, *Phys. Rev. B* **45**, 3749 (1992).
- [60] S. Andrieu, H. Fischer, M. Piecuch, A. Traverse, and J. Mimault, *Phys. Rev. B* **54**, 2822 (1996).
- [61] D. Tian, A. Begley, and F. Jona, *Surf. Sci. Lett.* **273**, 393 (1992).
- [62] I. Grigorov and J. Walker, *J. Appl. Phys.* **81**, 3907 (1997).
- [63] I. Grigorov, J. Walker, M. Hawley, G. B. adn M. Lütt, and M. Fitzsimmons, *J. Appl. Phys.* **83**, 7010 (1998).
- [64] I. Grigorov, I.-L. Siu, M. Fitzsimmons, and J. Walker, *Phys. Rev. Lett.* **82**, 5309 (1999).
- [65] A. Arrott, B. Heinrich, S. Purcell, J. Cochran, and L. Urquhart, *J. Appl. Phys.* **61**, 3721 (1987).
- [66] K. Ounadjela, P. Vennegues, Y. Henry, A. Michel, V. Pierron-Bohnes, and J. Arabski, *Phys. Rev. B* **49**, 8561 (1994).
- [67] L. Zhang, M. Kuhn, and U. Diebold, *Surf. Sci.* **371**, 223 (1997).
- [68] M. Albrecht, J. Pohl, H. Wider, E. Malang, J. Kohler, K. Friemelt, and E. Bucher, *Surf. Sci.* **397**, 354 (1998).
- [69] M. Sambì and G. Granozzi, *Surf. Sci.* **426**, 235 (1999).

- [70] S. Heinze, P. Kurz, D. Wortmann, G. Bihlmayer, and S. Blügel, *Appl. Phys. A* **75**, 25 (2002).
- [71] D. Wortmann, S. Heinze, P. Kurz, G. Bihlmayer, and S. Blügel, *Phys. Rev. Lett* **86**, 4132 (2001).
- [72] S. Handschuh and S. Blügel, *Solid State Commun* **105**, 633 (1998).
- [73] T. Asada, S. Blügel, G. Bihlmayer, S. Handschuh, and R. Abt, *J. Appl. Phys.* **87**, 5935 (2000).
- [74] S. Mirbt, O. Eriksson, B. Johansson, and H. Skriver, *Phys. Rev. B* **52**, 15070 (1995).
- [75] R. Wu and A. Freeman, *Phys. Rev. B* **51**, 17131 (1995).
- [76] O. Elmouhssine, G. Moraitis, C. Demangeat, and J. Parlebas, *Phys. Rev. B* **55**, R7410 (1997).
- [77] R. Pfandzelter, T. Igel, and H. Winter, *Surf. Sci.* **389**, 317 (1997).
- [78] F. Hillebrecht, C. Roth, R. Jungblut, E. Kisker, and A. Bringer, *Europhys. Lett* **19**, 711 (1992).
- [79] R. Jungblut, C. Roth, F. Hillebrecht, and E. Kisker, *J. Appl. Phys* **70**, 5923 (1991).
- [80] D. Venus and B. Heinrich, *Phys. Rev. B* **53**, R1733 (1996).
- [81] R. Pfandzelter, T. Igel, and H. Winter, *Phys. Rev. B* **54**, 4496 (1996).
- [82] A. Davies, J. Stroschio, D. Pierce, and R. Celotta, *Phys. Rev. Lett.* **76**, 4175 (1996).
- [83] T. Igel, R. Pfandzelter, and H. Winter, *Surf. Sci.* **405**, 182 (1998).
- [84] P. Lang, V. S. Stepanyuk, K. Wildberger, R. Zeller, and P. H. Dederichs, *Solid State Commun.* **92**, 755 (1994).
- [85] B. Nonas, I. Cabria, R. Zeller, P. H. Dederichs, T. Huhne, and H. Ebert, *Phys. Rev. Lett.* **86**, 2146 (2001).
- [86] V. S. Stepanyuk, W. Hergert, K. Wildberger, R. Zeller, and P. H. Dederichs, *Phys. Rev. B* **53**, 2121 (1996).
- [87] K. Wildberger, V. S. Stepanyuk, P. Lang, R. Zeller, and P. H. Dederichs, *Phys. Rev. Lett.* **75**, 509 (1995).
- [88] O. Eriksson, R. C. Albers, and A. M. Boring, *Phys. Rev. Lett.* **66**, 1350 (1991).
- [89] R. Wu and A. J. Freeman, *Phys. Rev. B* **45**, 7222 (1992).